High-Resolution Analysis of Snow Albedo Interactions in the Arctic

by

Daniel Hogg

A thesis
presented to the University of Waterloo
in fulfillment of the
thesis requirement for the degree of
Master of Mathematics
in
Applied Mathematics

Waterloo, Ontario, Canada, 2022

Author's Declaration

I hereby declare that I am the sole author of this thesis. This is a true copy of the thesis, including any required final revisions, as accepted by my examiners.

I understand that my thesis may be made electronically available to the public.

Abstract

The Snow Albedo Feedback (SAF) is an important contributor to Arctic warming, however models disagree significantly on the strength of this effect. Previous work has investigated the influence of vegetation on surface albedo, however the accuracy has been limited by the resolution of model output. In this work, we perform a pan-Arctic survey using Moderate Resolution Imaging Spectroradiometer (MODIS) remote sensing data and Coupled Model Intercomparison Project (CMIP6) model output, to perform a comprehensive analysis of the effects of vegetation on SAF. We computed pan-Arctic composites of MODIS observational data at the 500m scale and compared the results with the CMIP6 ensemble.

Using MODIS data, we found a mean SAF of -2.17 $\% \cdot K^{-1}$ from April-July over the climatological period 2001-2019, which is stronger than predicted by the CMIP6 intermodel mean. Additionally, we identified the source of this discrepancy - models currently do not adequately capture the dynamics of late-season melt-off in the high Arctic grassland and barren regions, which results in an underestimate of SAF. In this work, we demonstrate that land cover changes have a small but nonzero ($\leq 10\%$) contribution to overall changes in SAF on the timescale of decades, indicating the importance of dynamic vegetation models. Furthermore, we identify upscaling resolution as a major source of local error in SAF, however due to cancellation of errors this has minimal impact on estimates of pan-Arctic mean SAF. Finally, we identify a logarithmic relationship between LAI (Leaf Area Index) and SAF. This work can benefit modelling groups seeking to better capture SAF dynamics, by explaining SAF errors in terms of vegetation dynamics, and by demonstrating the existence of spatial structure in SAF fields at sub-model grid scales.

Acknowledgements

Firstly, I would like to thank my parents for always encouraging mathematical and scientific curiosity throughout my childhood, and my brother and sister for their support.

I also thank my supervisor Prof. Christopher Fletcher for his immense support and guidance over the course of my thesis. I have greatly appreciated your patience and willingness to explore unconventional approaches.

Additionally, I thank the members of my research group including Tyler Herrington, Neha Kanda, Fraser King and Jack Virgin for the numerous helpful discussions over the course of the past two years.

Table of Contents

List of Figures

List of Tables

List of Abbreviations

AVHRR Advanced Very High Resolution Radiometer. 36

BSA Black-sky Albedo. 13

CESM Community Earth System Model. 8

CLASS Canadian Land Surface Scheme. 49

CLM Community Land Model. 8

CMIP6 Coupled Model Intercomparison Project Phase 6. 12

ESM Earth System Model. 7

LAI Leaf Area Index. 4

LSM Land Surface Model. 7

LST Land Surface Temperature. 12

MODIS Moderate Resolution Imaging Spectroradiometer. 12

NDVI Normalized Difference Vegetation Index. 5

SAF Snow Albedo Feedback. 2

WSA White-sky Albedo. 13

List of Symbols

K Number of columns of spatial composite matrix. 20

L Number of rows of spatial composite matrix. 20

N Number of vegetation subtypes. 19

$\alpha_{\mathbf{sfc}}$ Land surface albedo reperesenting the fraction of reflected radiation.. 2

$\mathbf{A_{i,t}}$ Area covered by a given vegetation subtype i in year t, with $A_{i,t} = \mathrm{Area}(\Omega_{i,t})$. 20

$\cap$ Set union. 17

$\cup$ Set intersection. ix, 18

$\gamma_{i,t}$ Area fraction for a given vegetation subtype for year t, defined by $\frac{A_{i,t}}{A}$ where A is the total area of the domain Ω. 21

κ_i Snow Albedo Feedback coupling coefficients $\kappa_1, \kappa_2, \kappa_3, \kappa_4$ defined in [2]. 6

NET Total Snow Albedo Feedback (SAF), represented as a finite difference $\Delta\alpha_{\mathrm{sfc}}/ < \Delta T >$. 42

Ω_i A subset of the domain Ω corresponding to the vegetation subtype with index i.. 19

Ω A general domain, which in this thesis we assume to be a subset $\Omega \subset \mathcal{R}^2$. 17

S Snow cover fraction, represented as a value $S \in [0,1]$. ix, 7

$\subseteq$ Subset. 17

T_s Surface Temperature. ix, 7

Chapter 1

Introduction

The Arctic is currently in a critical period for climate change. Over the past several decades, and projected into the future, we observe rapid change across all metrics, from temperature to ice coverage. The Arctic is warming up considerably faster than the rest of the world [4], with $2 - 3°$ C of warming observed since the 19th century. This is accompanied by well-documented decreases in sea ice coverage [5], as well as receding glaciers in Greenland [6] and the Canadian Arctic archipelago.

Of particular interest is the Snow Albedo Feedback (SAF), which contributes to an amplification of warming in the Arctic. The surface albedo α measures the proportion of reflected solar radiation, and is a key parameter determining the radiative balance. Presently, models differ significantly in their estimates of the magnitude of the SAF [7] [8]. This provides motivation for a better understanding of the relationship between snow cover, vegetation and surface albedo, as these surface properties all influence the SAF. In this work, we perform a full investigation of the link between vegetation and SAF using a combination of remote sensing data and model output.

1.1 Surface Albedo

The radiative energy budget of Earth can be decomposed into longwave (terrestrial) and shortwave (solar) radiation. In this work, we limit the scope of our investigation to incoming solar radiation and its interactions with the Earth's surface.

Definition 1 ***Surface albedo*** α_{sfc} *is defined as the ratio of integrated upwelling spectral irradiance* $E_{u\lambda}$ *and downwelling spectral irradiance* $E_{g\lambda}$*, where the integration is performed*

1

over a wavelength band $[\lambda_1, \lambda_2]$ *[9].*

$$\alpha_{sfc} = \frac{\int_{\lambda_1}^{\lambda_2} E_{u\lambda} d\lambda}{\int_{\lambda_1}^{\lambda_2} E_{g\lambda} d\lambda} \tag{1.1}$$

The full treatment of the interaction between an optical surface and light requires the treatment of bidirectional reflectance [10], which is a probability distribution over all incident and reflected angles. Surface albedo provides a convenient way to integrate out these angular terms into a single scalar quantity that represents the proportion of radiation that is absorbed a given point on the optical surface. Surface albedo is a key determinant of the Earth's climate, as regions with low albedo absorb more radiation and thus contribute to the net global warming.

1.2   Vegetation as a Predictor of Albedo

Snow and vegetation together form the optical surface where radiation is either reflected, emitted or absorbed. Surface albedo directly impacts the rate at which incoming short-wave radiation is reflected or absorbed. The optical properties of the Earth's surface can also influence the emissivity of outgoing terrestrial radiation [11], however this is outside the scope of this thesis. The primary interaction between snow and vegetation is through masking, where snow is deposited on top of the vegetation layer. A consequence of this interaction is that the surface albedo is highly dependent on the vegetation, and motivates the use of vegetation indicators to predict albedo. Vegetation indicators are either categorical (discrete) or continuous.

Definition 2 *Vegetation Subtype is a discrete indicator, which takes a set of N vegetation categories and associates each pixel of a remote-sensing or model dataset to a distinct vegetation category.*

Loranty (2011) [1] demonstrated that Arctic regions of different vegetation subtype show different seasonal cycles of albedo (reproduced in Fig.1.1). In this analysis, low-height vegetation subtypes such as sedge had $\alpha_{\max} = 0.757$, while forest regions have much lower maximum albedo with $\alpha_{\max} = 0.403$. More recent work [12] has shown that forested regions have albedo profiles that differ based on vegetation subtype. This motivates further investigation of the use of vegetation subtype as a predictor.

2
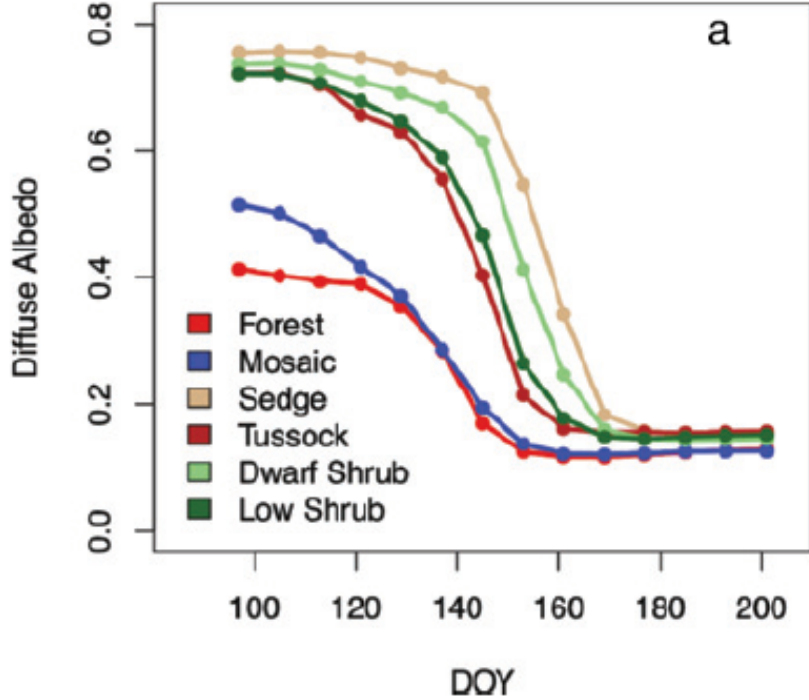
Figure 1.1: Albedo seasonal evolution closely resembles a logistic curve for each vegetation subtype, representing a transition from the snow-covered $\alpha_{\max}$ to the snow-free $\alpha_{\min}$ value once the spring melt-off has concluded. Original figure from [1].

Definition 3 *Leaf Area Index (LAI) is defined as the one-sided leaf area per unit ground surface area [13], in units of [m²/m²].*

Wang (2016) [3] performed an analysis using the Canadian Land Surface Scheme (CLASS) model [14], showing two key results. The first result is that the albedo of regions with low LAI are more sensitive to LAI errors than regions with high LAI. Secondly, Wang performed a model simulation demonstrating that reducing the LAI in the model (a simulation of deforestation) for taiga and tundra regions yielded higher albedo values, and hence a net cooling. However, similar investigations at tropical latitudes show that deforestation at lower latitudes yields a net heating effect [15] [16], given the absence of snow in equatorial regions.

3

Analysis of NDVI changes in the Arctic has been the subject of considerable study [17] [18]. Given the prominence of NDVI as a vegetation metric in the remote sensing literature, it is a natural candidate to consider for making predictions of albedo. However, previous results [19] have shown only a loose correlation ($R^2 = 0.58$) between NDVI and surface albedo, and thus we restrict our attention in this work to using vegetation subtype and LAI to predict surface albedo.

Definition 4 *The **Normalized Difference Vegetation Index (NDVI)** is a normalized metric of vegetation density derived from the difference between spectral reflectance in the near-infrared ρ_{nir} and red ρ_{red} bands. The reflectances are defined as the ratio between reflected and incident radiation within a given wavelength band.*

$$NDVI = \frac{\rho_{nir} - \rho_{red}}{\rho_{nir} + \rho_{red}} \tag{1.2}$$

By construction, this metric is bounded within the range $NDVI \in [-1, 1]$.

1.2.1 Effects of Arctic Greening on Surface Albedo

The Moderate Resolution Imaging Spectroradiometer (MODIS) operational data record from 2000-2021 has recorded large-scale vegetation shifts, including many studies which show widespread greening [20] [18]. While the vegetation changes have been extensively covered in the literature, the impact of these vegetation shifts on albedo has not been fully explored, which motivates an investigation of this mechanism. Arctic greening has typically been classified in the literature [21] as a function of NDVI, while we seek to investigate changes in albedo as a function of vegetation subtype (land cover shifts) and LAI (Arctic greening).

We have identified three important vegetation processes which are occurring in the Arctic and Taiga regions, which we propose have a significant effect on albedo. It is important to note that there is a coupling between all of these effects and snow, as mentioned in the previous section. All three of these effects must be considered as special cases of the overall greening trend. One of the primary goals of this thesis is to compute the effects of these trends on SAF.

1. Greening of the Arctic (barren regions becoming vegetated)

2. Greening of the Arctic (increased LAI in existing vegetated regions)

3. Transitions from one type of vegetation to another

1.3 Snow Albedo Feedback

The snow albedo feedback (SAF) [22] is a feedback process which affects snow cover in the Arctic. An intitial rise in temperature causes a decrease in snow cover S, which decreases the albedo, which again causes an increase in temperature, creating a feedback loop. Due to its role in Arctic amplification, the SAF has been the subject of considerable interest, both in terms of analytic calculations and model simulations. Thackeray's study defines the NET term [7] as the total derivative of surface albedo with respect to temperature, the formal definition of which is given below.

Definition 5 *Snow Albedo Feedback:* *The NET term represents SAF in terms of a total derivative in units of percent albedo change per Kelvin [% · K^{-1}]. The numerator α_{sfc} is a spatial field representing the monthly difference in albedo, and the denominator is the monthly temperature difference averaged over the pan-Arctic domain.*

$$\kappa_4 = NET = \frac{\Delta\alpha_{sfc}}{<\Delta T>} \tag{1.3}$$

In Definition 5, the angle brackets represent a spatial average over the entire pan-Arctic domain. As a point of clarification, in this work percent albedo change refers to an absolute change in albedo, where 1% corresponds to an albedo change of $\Delta\alpha_{\mathrm{sfc}} = 0.01$.

Qu and Hall (2007) [2] decomposed the SAF relationship between snow, surface temperature and surface albedo using four coupling coefficients κ_i. There are four physical effects, including the change in snow cover caused by temperature increase κ_1, changes in albedo due to snow masking κ_2, albedo shifts due to temperature-induced snowpack metamorphosis κ_3, and κ_4 measures increases in surface temperature due to radiative transfer induced by albedo change. We note that the κ_4 coefficient is exactly the NET term introduced in [7].

Having established the need for a more thorough investigation of the influence of vegetation on surface albedo α_{sfc}, the next step is an analysis of how vegetation modifies the interaction between snow cover, temperature and surface albedo. In Fig. (1.2), we extend the schematic diagram from [2] to illustrating the additional couplings that vegetation provides to the SAF. We theorize that vegetation has three distinct couplings to SAF; changes to vegetation subtype occurring over decades, vegetation-induced change in albedo, and changes to the snow fraction S caused by canopy masking.
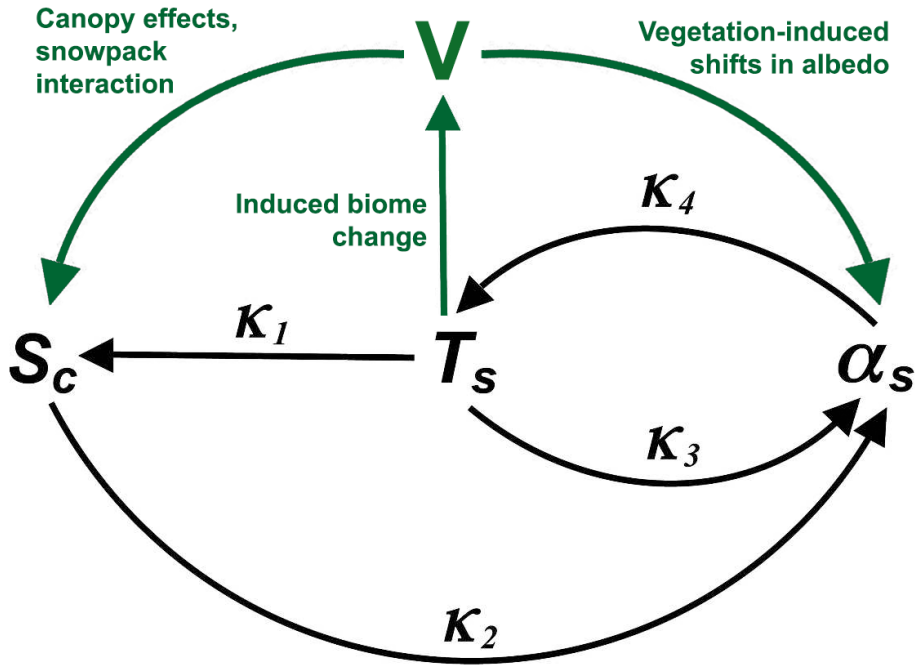
Figure 1.2: Diagram showing links between vegetation, surface temperature T_s, albedo and snow cover S. Original figure from [2]

1.4 Land Surface Models

Earth System Models (ESMs) are complex simulations of climate dynamics, which include many coupled sub-components. The Coupled Model Intercomparison Project (CMIP) is a set of ESMs, with the output data standardized for the purpose of comparison. One important component of these ESMs is Land Surface Models (LSMs), which simulate processes occurring at the Earth's surface such as the impacts of vegetation on the carbon cycle, evapotranspiration and surface albedo. Within these models, it is not possible to simulate all processes in terms of PDEs. The unresolved physics must be parametrized, so we instead have explicit parametrizations for certain components. In this work, we focus on investigating the parametrization of vegetation canopy effects on surface albedo.

An example of an ESM is the Community Earth System Model (CESM), for which Thackeray et al.[23] demonstrated the existence of vegetation-linked biases in surface albedo, specifically related to vegetation masking. Within the most recent version (CESM2) [24], the land dynamics are performed by Community Land Model 5 (CLM5) [25]. The link between land cover and surface albedo in CLM4.5 has been explored in Meier et al.[26]. The land and atmospheric simulations are coupled by means of atmospheric input such as pressure, temperature and CO_2 concentration. In return, the land model provides output such as diffuse and direct albedo, heat flux, and absorbed solar radiation.

Much recent work has been performed on soil hydrodynamics, biogeochemistry [27] and atmospheric coupling [28], in the context of investigating simulations of vegetation in land surface models. However, for the purpose of our investigation, we seek to understand the impacts of vegetation dynamics on albedo specifically. Therefore, we limit the scope of our analysis of vegetation to strictly the effects which modify the surface albedo. Within the context of vegetation-driven changes to vegetation, there are diverse characteristics which impact model behavior. These include plant functional type, crop functional type, leaf area index (LAI), vegetation height and canopy gap fraction.

1.4.1 Canopy Effects

The interception of snowfall by a vegetation canopy has significant effects on the resulting surface albedo. Furthermore, models differ significantly in their representation of canopy effects. A framework for classifying parametrizations within LSMs was introduced by Qu & Hall in [2], and was expanded by Essery [29]. In this framework, canopy parametrizations are separated into four types, with Type 1 the most complex (full simulation of radiative transfer), and Type 4 the most simplified parametrization (assuming albedo is independent of vegetation).

Type 3 parametrizations involve a simple weighted average where the surface albedo is sum of the snow albedo α_{snow} and the land albedo α_{land}, weighted by the snow cover fraction S.

$$\alpha_{\text{sfc}} = \alpha_{\text{snow}}S + \alpha_{\text{land}}(1 - S) \tag{1.4}$$

Although some research in this domain has previously focused on either vegetation [1] [30] or snow exclusively, more recent work has focused on modeling the effects of snow and vegetation together. A recent paper by Essery [29] performed a detailed analysis of canopy effects on albedo. The ECHAM5 climate model [31] is an ESM which includes treatment of the canopy as a separate layer from the ground, which corresponds to a Type

2 parametrization. This involves a two-level approximation, where the gap fraction f_g represents the probability of a photon passing through the canopy layer and reaching the ground [32]. This parametrization is linear with respect to snow cover f_s, canopy snow cover f_c, and gap fraction f_g.

$$\alpha_{\text{sfc}} = f_g\Big[(1 - f_s)\alpha_{g0} + f_s\alpha_{gs}\Big] + (1 - f_g)\Big[(1 - f_c)\alpha_{c0} + f_c\alpha_{cs}\Big] \tag{1.5}$$

The reflection of incoming solar radiation incident onto a vegetated surface either partially or fully covered in snow is an instance of thermal radiation transfer in the context of a participating medium. The full geometry of a snowbank with complicated geometry on top of a non-uniform vegetated surface is too computationally expensive to model directly, therefore some simplifying assumptions must be made.

1.4.2 Intermodel Spread in SAF

Accurate modelling of the SAF is an ongoing challenge for land surface models. The intermodel spread in the CMIP5 ensemble [33] ranges from -0.67 to $-1.66\% K^{-1}$. Given the importance of the snow albedo feedback in determining the strength of Arctic warming, this spread creates large uncertainty in climate projections.

Previous work [8] [34] has suggested that the differences in how these models treat vegetation is a significant source of uncertainty in albedo. This provides clear motivation for further investigation into the role of vegetation variability on albedo, and by extension the SAF. Additionally, we wish to investigate the SAF spread in land surface models by using a simplified modelling framework.

Existing parametrizations of surface albedo within CMIP5 models are quite complex in that each model uses a different combination of schemes for representing land, snow albedo and vegetation masking. Qu and Hall [2] classified canopy parametrizations into four different categories, organized by complexity of the parametrization of snow-vegetation interaction. A key result from an analysis of SAF spread in CMIP5 models [33] was the discovery that more complex parametrizations did not necessarily correspond better to observations, and in fact some of the least-performant models used a full radiative transfer model to account for the canopy interaction.

Hall and Qu (2006) [35] introduced the notion of emergent constraints, which is the approach of using an ensemble of climate models to derive an empirical relationship between current climate observations and future predicted quantities [37]. This technique has been applied to constrain uncertainties on effects such as snow albedo feedback [36] and sea-ice

albedo feedback [38]. In contrast, a complete understanding of SAF for individual models would require detailed perturbed physics experiments for each model. Emergent constraints seek to leverage an ensemble of climate models in order to determine relationships between climate quantities without having to perform computationally expensive diagnostics of individual models.

Our aim is to create a simplified diagnostic framework that can be used to identify issues with this entire ensemble of land surface models. The advantage of this diagnostic approach is that we can isolate specific physical processes (such as decadal land cover changes, canopy interactions, or the timing of spring melt-off) and see how well each model simulates these processes. The goal of this diagnostic framework is to identify specific issues in the existing ESM ensemble that lead to a large spread in the SAF.

In addition to categorizing the relevant physical mechanisms behind vegetation interactions, we are also interested in identifying the most relevant physical scale for this process. Given that the surface albedo depends critically on local surface characteristics, we expect albedo variability at the stand scale (≈50m). Given that the typical ESM grid cells are on the order of 100km, this provides an opportunity to use remote sensing data at the highest available resolution to determine SAF with greater accuracy. The computation of SAF at the 500m scale has not been performed previously in the literature, providing a clear motivation for a high resolution pan-Arctic study.

1.5 Research Questions

This Thesis is organized around the following three questions, each with a corresponding set of testable hypotheses, relating to a specific theme of <u>variability</u>, <u>resolution</u> and <u>model spread</u>.

1. What is the link between variability in Arctic vegetation and surface albedo on timescales from days to decades?

   Hypothesis 1 *Vegetation subtype is a strong predictor of surface albedo in that variability within a vegetation subtype is less than variability between subtypes.*

   Hypothesis 2 *Change in vegetation on a decadal scale has a detectable impact on surface albedo. We classify these changes as land-cover driven shifts in albedo.*

2. What is the influence of grid resolution on local and global (pan-Arctic mean) errors in SAF?

Hypothesis 3 *Given the spatial heterogeneity in vegetation subtypes at the 500m scale, we predict similar high-resolution spatial structure in SAF at sub-model grid scales.*

Hypothesis 4 *Existing model grid sizes are too coarse to fully capture observed land albedo interactions. We predict this introduces a significant error that may contribute to intermodel spread in SAF.*

3. To what extent do vegetation characteristics such as vegetation subtype and leaf area index explain the intermodel spread in SAF?

   Hypothesis 5 *Given the link between vegetation and surface albedo, we predict that model errors in representing vegetation subtype and leaf area index are linked to errors in SAF.*

Chapter 2

Data and Methods

2.1 Data Summary

Satellites such as MODIS (Moderate Resolution Imaging Spectroradiometer) and Sentinel-3 provide researchers with access to remote sensing datasets for a variety of observed quantities. These include LST (Land Surface Temperature), albedo, NDVI, among others. A key feature of these datasets is their high resolution, which permits investigation of surface phenomena down to the 500m scale.

In contrast, numerical climate models are run at much larger resolutions, with the latitudinal resolution of models in the CMIP6 (Coupled Model Intercomparison Project Phase 6) ensemble ranging from 78km to 313km per grid cell. This chasm between the resolution of remote sensing data and models provides both challenges and opportunities, particularity for the case of characterizing correlations and physical processes. We introduce methods that aim to use both high-resolution remote sensing data and CMIP6 model output to investigate the dynamics relating snow cover, vegetation and surface albedo.

In this work, the pan-Arctic spatial domain is all land surface north of 60°N, excluding Greenland. We exclude Greenland using spatial masking to maintain consistency with the existing literature [22]. The rationale behind this exclusion is due to the almost complete lack of vegetation on Greenland, as well as the fact that different models are not consistent in how the Greenland ice sheet is represented. This choice of spatial domain is applied to both the remote sensing and model analysis.

2.1.1 Remote Sensing Data

The primary remote sensing dataset used in this work is MODIS (Moderate Resolution Imaging Spectroradiometer), an instrument onboard the Terra and Aqua satellites [39], and the selected variables are summarized in Table 2.1. MODIS products have global coverage, with over 20 years of operational data. Given that we wish to perform a pan-Arctic analysis on the impact of slowly-changing vegetation on albedo over a multi-decadal timescale, this high degree of spatial and temporal availability makes the MODIS dataset well-suited for our use case.

The binary data collected by MODIS sensors is referred to as Level-0 data. This input data is then converted into calibrated radiance fields (Level-1 data) [40]. Finally this information is processed into a set of gridded geophysical parameters (classified as Level-2 and Level-3 products, indicating a higher degree of post-processing). One limitation of this work is that we use the post-processed Level-3 products as a starting point for our analysis, and therefore we assume the reliability of the MODIS data processing, given that we do not deal with the radiances directly.

Given that our goal is better characterization of surface albedo, we can consider two kinds of limitations. The first is **observational**, in that we might be limited by the availability of data or the temporal and spatial resolution of the datasets in question. Given that MODIS data is available at a high spatial resolution (1km or 500m, depending on the product), and is available over a 20-year time period, we do not face many observational limitations.

Another limitation is **computational**, in that it is not feasible to run numerical climate models at the resolution of the availability of remote sensing data. As an alternative approach, we plan to analyze subgrid parametrizations of surface albedo, such that the high-resolution vegetation datasets can be fully utilized. Additionally, we aim to investigate correlations between the MCD12Q1 (Land Cover Type) and MCD43A3 (Surface Albedo) datasets.

The albedo fields provided by MODIS are given in the MCD43A3 dataset, which includes both **white-sky albedo (WSA)** and **black-sky albedo (BSA)**. WSA represents albedo for completely diffuse incoming radiation, while BSA is the albedo of completely direct incident radiation [9]. In order to maintain consistency with previous work [1], we use white-sky albedo (diffuse) to remove the dependence on solar zenith angle [42]. There exists a third type called **blue-sky albedo (BSA)**, which is a linear combination of WSA and BSA weighted to simulate realistic atmospheric conditions, however MODIS does not provide a blue-sky albedo product.

Key	Dataset Name	Frequency	Size	Resolution
MCD12Q1	Terra+Aqua Land Cover Type	Yearly	5.5 GB	500m
MCD43A2	Terra+Aqua Albedo Quality	Daily	6.2 TB	500m
MCD43A3	Terra+Aqua Albedo	Daily	20.9 TB	500m
MOD10A1	Snow Cover	Daily	2.0 TB	500m
MOD11A1	Terra Land Surface Temp.	Daily	1.0 TB	1km
MOD13A3	Terra Vegetation Indices	Monthly	98 GB	1km
MOD15A2H	Terra Leaf Area Index	8-Day Mean	62 GB	500m

Table 2.1: Table of MODIS datasets used so far in this work. Note that the sizes are for all tiles in the operational history (2001-2019) over the entire pan-Arctic domain. The albedo datasets are too large to store directly, but we plan to work around this by storing only a subset of the albedo channels.

For our analysis of vegetation, we use two separate products. The first, MCD12Q1, provides a set of land cover classifiers. There are five distinct classification schemes in this dataset. Currently, we use the Annual Plant Functional Types classification [43], as its categories correspond best to the existing literature on forest albedo [29]. The second is MOD15A2H, a dataset of LAI values used for comparison with model output.

2.1.2 Model Data

The Coupled Model Intercomparison Project Phase 6 (CMIP6) [44] is the latest iteration of the CMIP project, which seeks to compare the model outputs from a collection of numerical climate models. The CMIP6 ensemble is the current state-of-the-art in coupled climate models in terms of resolution and physical parametrizations.

Given the importance of resolution in climate models, statistical [45] and dynamical downscaling [46] techniques have been developed. Statistical downscaling attempts to improve the resolution of global climate models by using historical meteorological observations. Dynamical downscaling involves using a global climate model to set the boundary conditions of a higher-resolution regional climate model. Statistical downscaling does not necessarily help constrain the intermodel spread in SAF, as we are still left with the challenge of spread coming from different vegetation parametrizations. For dynamical downscaling, the lateral boundary conditions coming from the global climate model would still be subject to the same resolution-limited effects. For these reasons, we do not employ downscaling in our analysis of SAF.

To maintain consistency with the remote sensing analysis, we choose a spatial domain that includes all land area north of 60°. For the temporal domain, we have selected 2001-2014 for the model comparisons, as this is the maximum temporal overlap between CMIP6 model output and remote sensing data availability.

The CMIP6 experiment we investigated was **AMIP** (Atmospheric Model Intercomparison Project), the data availability of which are summarized in Tables 2.2. The temporal domain of the CMIP6 AMIP simulations is from 1979-2014. A key feature of the AMIP experiments is that SST (Sea Surface Temperature) and SIC (Sea Ice Concentration) are prescribed to historical values [44], while allowing land/atmosphere to evolve freely.

Given the SST and SIC forcings to historical temperatures, this makes AMIP a good comparison to the historical MODIS record. Of the 33 models in the AMIP ensemble, we selected all models with LAI data availability, creating a 24-member ensemble to examine the relationship between LAI and SAF.

Table 2.2: Data Availiblity for AMIP Model Runs (2001-2014)

Model Name	Lon×Lat	TS	RSDS/RSUS	Veg. Subtype	LAI
1. ACCESS-CM2	1.88°×1.25°	✓	✓	✓	−
2. ACCESS-ESM1-5	1.88°×1.24°	✓	✓	✓	✓
3. BCC-ESM1	2.81°×2.81°	✓	✓		✓
4. CAMS-CSM1-0	1.13°×1.13°	✓	✓	−	✓
5. CESM2-WACCM	1.25°×0.94°	✓	✓	−	✓
6. CESM2	1.25°×0.94°	✓	✓	−	✓
7. CIESM	1.25°×0.94°	✓	✓	−	✓
8. CMCC-CM2-HR4-8	1.25°×0.94°	✓	✓	−	✓
9. CMCC-CM2-SR5-0	1.25°×0.94°	✓	✓	✓	✓
10. CanESM5	2.81°×2.81°	✓	✓	−	✓
11. E3SM-1-0	1.00°×1.00°	✓	✓	−	✓
12. EC-Earth3	0.70°×0.70°	✓	✓	−	−
13. EC-Earth3-AerChem	0.70°×0.70°	✓	✓	−	−
14. EC-Earth3-CC	0.70°×0.70°	✓	✓	✓	✓
15. EC-Earth3-Veg	0.70°×0.70°	✓	✓	−	✓
16. FGOALS-g3	2.00°×2.25°	✓	✓	−	✓
17. GFDL-ESM4	1.25°×1.00°	✓	−	−	−
18. GISS-E2-1-G	2.50°×2.00°	✓	✓	−	✓
19. IITM-ESM	1.88°×1.91°	✓	✓	−	−
20. INM-CM4-8	2.00°×1.50°	✓	✓	−	✓
21. INM-CM5-0	2.00°×1.50°	✓	✓	−	✓
22. IPSL-CM6A-LR	2.52°×1.25°	✓	✓	−	✓
23. KACE	1.88°×1.25°	✓	✓	−	−
23. KIOST-ESM	1.88°×1.88°	✓	✓	−	✓
24. MIROC6	1.41°×1.41°	✓	✓	−	−
25. MPI-ESM-1-2-HAM	1.88°×1.88°	✓	✓	−	✓
26. MPI-ESM1-2-HR	0.94°×0.94°	✓	✓	−	✓
27. MPI-ESM1-2-LR	1.88°×1.88°	✓	✓	−	✓
28. MRI-ESM2	1.13°×1.13°	✓	✓	−	−
29. NESM3	1.88°×1.88°	✓	✓	−	−
30. NorCPM1	2.50°×1.88°	✓	✓	−	−
31. NorESM2-LM	2.50°×1.88°	✓	✓	−	✓
32. SAM0-UNICON	1.25°×0.94°	✓	✓	−	✓
33. TaiESM1	1.25°×0.94°	✓	✓	−	✓

2.2 Partitions of a General Domain

Both observational and model data are stored in gridded datasets[1], corresponding to some 2D projection. This projection is specified in the native projection coordinates $(x, y) \in \mathbb{R}^2$, which is locally isomorphic to some subset of the Earth's surface $\Omega \subseteq S^2$. For the purpose of this document, the methods we introduce are projection-independent. The only assumption we make regarding the projection is each pixel of the gridded datasets contain approximately the same area. However, this does not hold in all cases, longitude-latitude grids are an example of when this assumption is violated. If the projection produces pixels of different areas (in the gridded datasets), a set of weights w_{kl} would be required to ensure normalization.

We consider the case of a general domain Ω, which represents a subsection of the Earth's surface. Furthermore, in this work we consider only surface effects, which allows us to consider only 2D partitions, and neglect the complications associated with multiple height levels (for example, atmospheric models contain many vertical levels). Additionally, we allow our domain to be non-contiguous, as this reflects the geography of many regions such as the Canadian Arctic Archipelago.

We take as a starting point a matrix representation $A \in M_{kl}(\mathbb{R})$ of some remote sensing dataset. An example of such a dataset would be LST (Land Surface Temperature), with the elements a_{kl} corresponding to temperature values of each pixel of the projection. Next, we introduce a **partition** of this domain.

Definition 6 *A **partition**[2] of a spatial domain Ω is a set of M non-overlapping subsets Ω_i, which satisfy the following constraints:*

1. The union of all subsets is the entire domain

$$\Omega = \bigcup_{i=1}^{M} \Omega_i \tag{2.1}$$

2. The intersection of any two subsets has zero area (meaning that the subsets share at most a border).

---

[1] For models, the underlying equations are solved at the scale of the model grid. For remote sensing data, typically the source resolution of the instrument is aggregated into a product resolution (for example, 500m in the case of the land cover product MCD12Q1).

[2] This notion of partition differs slightly from the strict topological definition provided in [47]. We relax the condition $\Omega_i \cap \Omega_j = \varnothing$ to allow for an infinitesimal overlap at the boundaries. In practice, these definitions are equivalent for our purposes, as the boundary intersections have zero area and thus do not contribute to our analysis.

$$\int_{\Omega_i \cap \Omega_j} d\Omega = 0 \qquad\qquad (2.2)$$
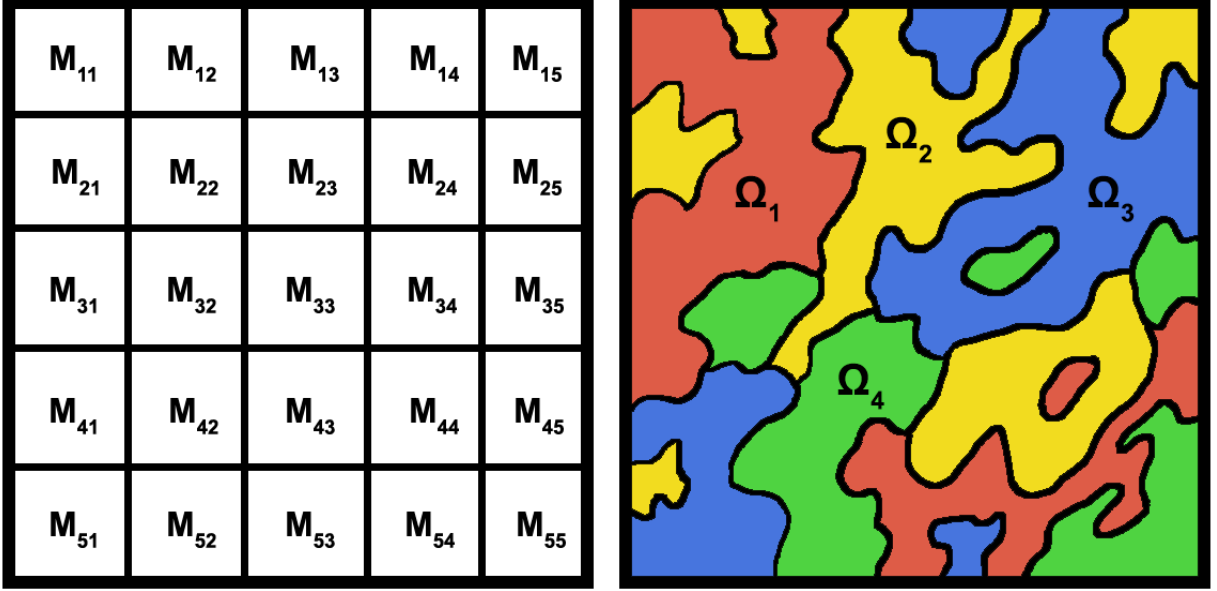
Figure 2.1: Schematic diagram illustrating the difference between a regular model grid (on the left) and a **partition**, as introduced in Definition 1. Here we have a partition of a rectangular domain Ω into four subsets Ω_1 (orange), Ω_2 (yellow), Ω_3 (blue), and Ω_4 (green). We observe that these subsets Ω_i are non-contiguous, and the union is equal to the entire domain, i.e. $\Omega = \Omega_1 \cup \Omega_2 \cup \Omega_3 \cup \Omega_4$.

This type of partition provides several key advantages. First, we note that the subsets Ω_i need not be contiguous, which allows us to create partitions that correspond to the underlying surface characteristics. In contrast, the regular lines of a model grid cut across these classifications. Secondly, this type of partition allows us to trace contours at the full resolution of the remote sensing dataset at the 500m or 1km level. A schematic showing a comparison between model grid cells and our partition is shown in Fig.2.1. Finally, this is a general method that can be applied to land surface problems generally, and is not limited to applications in the Arctic (although that is the focus of this work).

In later sections, we introduce a partition according to vegetation subtype, in which each subdomain corresponds to a distinct vegetation class, such as evergreen forest or

shrubland. As we expect that the surface albedo α_{sfc} of each biosphere will behave similarly, this motivates a decomposition in terms of vegetation subtype. In contrast, we expect the surface albedo to vary considerably over a model grid cell. We can also consider similar partitions based on other surface properties, such as elevation or land surface temperature[3].

Although this definition is provided for the continuous case, in practice all remote sensing datasets are provided in gridded representation at a finite resolution. These partitions are implemented by applying masks to a gridded array of spatial data. In the discrete case, an element Ω_i of the partition is the set of all pixels corresponding to category i. In order to use this partition scheme, we must assume that each pixel corresponds to exactly one category.

2.2.1   Partition: Vegetation Subtype

For the categories of vegetation subtypes, we specify these sub-regions as $\left\{ \Omega_1, \cdots, \Omega_N \right\}$. This decomposition provides much more flexibility, as there are a variety of vegetation classifiers available. To each vegetation subtype we associate a (potentially non-contiguous) region Ω_i.

The MODIS MCD12Q1 dataset provides five distinct land cover classifications. In this work, we use the decomposition specified by the Annual Plant Functional Types classification, which separates the Arctic domain into the N = 6 categories of evergreen forest, deciduous broadleaf, deciduous needleleaf, shrub, grass and barren regions. The Circumpolar Arctic Vegetation Map (CAVM) [48] includes a vegetation classification with $N = 26$ distinct subtypes. However, the domain specified in the CAVM does not cover the pan-Arctic domain north of 60°N, therefore we cannot use this classification as part of our analysis.

2.3   Pan-Arctic Composites

One of the primary methods used in this work is the construction of pan-Arctic composites consisting of all land surface area north of the 60N parallel. We generate and store these composites as large matrices in the MODIS Sinusoidal projection [49]. This equal-area projection consists of appending all individual MODIS tiles into a joint spatial product, which is then analyzed using the following methodology.

---

[3]For the case of a continuous variable (such as NDVI or temperature), we must bin the data into M discrete bins in order to perform this decomposition.

2.3.1   Methodology for Generating Composites

Each of the composites are produced at the maximum spatial and temporal resolution available over the 2001-2019 period of study, which is 500m for Land Cover and Surface Albedo, and 1km for the Land Surface Temperature (LST) product. Since land cover is a slowly-varying quantity, MODIS provides MCD12Q1 as a yearly product, while the Albedo and LST are available as daily products. For the Albedo and LST composites, we compute a daily albedo composite from 2001-2019, over the March-August window. This temporal window is chosen as it fully captures the spring melt cycle, which is the primary physical process for the Snow Albedo Feedback.

Despite these differences in temporal and spatial availability, the basic methodology for constructing the composites is the same in all cases, and is outlined in this section.

1. Construct a pan-Arctic K × L composite, which consists of all MODIS tiles at a single timestep for a given product (Land Cover, Albedo or LST).

2. Perform a spatial mask to exclude bodies of water and Greenland. We have excluded Greenland from all of our analysis in order to maintain consistency with the methodology of the existing literature [7]. The motivation for this exclusion is that Greenland is primarily covered by permanent glaciers, and thus does not have a seasonal melt cycle as we see in non-glaciated regions.

3. Exclude invalid pixels from the analysis. This is primarily applicable to the MCD43A3 product, which cannot resolve the surface albedo when there is cloud cover. For invalid land cover pixels, we note that although these categories are changing with respect to time, the fractional area change due to invalid and water pixels over the pan-Arctic domain is 0.0024%, and thus to a very good approximation we can consider the total land area as a constant.

We then use these fields as a starting point for further analysis. The procedures for temporal, spatial and climatological means are described in §2.3.2. For the analyses consisting of the entire domain, we exclude only Greenland and bodies of water. For the case of subtype analysis (i.e., using the partitioning scheme described in §2.2.1), we first perform a spatial partition into land cover types whose regions are represented by Ω_i, with the index i corresponding to each vegetation subtype. Next, we define the area $\mathbf{A_{i,t}}$ of a partition using the following expression:

$$A_{i,t} \equiv \text{Area}(\Omega_{i,t}) \tag{2.3}$$

19

We additionally define an area fraction $\gamma_{i,t}$ for a given vegetation subtype i for a particular year t, corresponding to the fraction of the total domain area A.

$$\gamma_{i,t} \equiv \frac{A_{i,t}}{A} \tag{2.4}$$

Furthermore, we construct these vegetation partitions in the temporal domain 2001-2019. Since land cover changes are small but nonzero, we obtain different partitions for each year. Symbolically, we can represent the changes in land cover fractions as the following derivative:

$$\frac{d}{dt}\frac{\text{Area}(\Omega_i)}{A} = \frac{d\gamma_i}{dt} \neq 0 \tag{2.5}$$

We wish to separate effects relating to change in land cover type (i.e. vegetation composition change) from changes within a vegetation subtype. The methodology used for subtype analysis is that we construct a vegetation mask for each subtype that consists of all pixels which have not undergone land cover change. That is, when analyzing the results for a given subtype (evergreen, deciduous needleleaf, deciduous broadleaf, shrub, grassland or barren) Ω_i, we analyze only pixels that were consistently one type of vegetation throughout the entire data record 2001-2019. This allows us to separately examine effects driven by land cover changes from effects within a vegetation type. Furthermore, an analytic scheme to decompose these effects is shown in more detail in §2.5.

In addition to these vegetation masks, we also construct regional spatial masks in order to separate results by region (Eurasia and North America, as well as an overall analysis of the pan-Arctic domain).

2.3.2 Albedo Composites

In this analysis, we seek to characterize the spatial and temporal variance of the surface albedo in terms of the standard deviation for each vegetation subtype. This analysis is required in order to justify to what extent our assumption (that albedo and SAF can be effectively decomposed by vegetation subtype) is valid.

Having established the procedure for generating albedo composites in §2.3, we take the daily albedo composites as a starting point for the following analyses. In order to determine the spatial variance, we first take the climatological mean for each day over the index set of years (2001-2019). We then obtain a spatial variance for each subtype by taking the standard deviation of all spatial points within a given vegetation subtype region Ω_i.

2.3.3 Field Averaging

In this section, we introduce a set of definitions to show exactly how the temporal, spatial and climatological means are calculated for each quantity of interest. First, we consider some field $\alpha(x, y, t)$ which has some spatial and temporal profile. Here α denotes albedo but these definitions apply to any GIS variable defined over a spatial grid.

Definition 7 *We denote the **spatial average** of a given variable $\alpha(x, y, t)$ as:*

$$\langle \alpha(x, y, t) \rangle = \frac{1}{A} \int_{\Omega} \alpha(x, y, t) dA \tag{2.6}$$

The angle brackets denote a spatial mean, converting functions of (x, y, t) into functions of t only by taking the spatial mean at each timestep over the domain Ω.

Definition 8 *We denote the **temporal average** of a given variable $\alpha(x, y, t)$ as:*

$$\bar{\alpha}(x, y) = \frac{1}{T} \int_{0}^{T} \alpha(x, y, t) dt \tag{2.7}$$

Furthermore we note that the temporal average transforms $\alpha(x, y, t)$ into a function of space only $\alpha(x, y)$ which has been temporally averaged at each point in the domain.

Definition 9 *We denote the **climatological average** of a given variable $\alpha(x, y, t)$ as the mean over an index set of N years. In this context, $\alpha_i(x, y, t)$ denotes the albedo for the ith year.*

$$\alpha(x, y, t) = \frac{1}{N} \sum_{i}^{N} \alpha_i(x, y, t) \tag{2.8}$$

Furthermore we note that the climatological average is, like its input functions $\alpha_i(x, y, t)$ also a function of three variables (x, y, t).

2.4 SAF Methodology

For our analysis of SAF, we use the daily pan-Arctic composites of albedo and snow cover to generate monthly averages. As part of our methodology, we look at only land pixels, and mask out Greenland from both our albedo field and the Land Surface Temperature spatial average. The data processing procedure is as follows:

1. Create daily composites of Land Cover Type (MCD12Q1), LST and Albedo over the entire data period (2001-2019)

2. Create a spatial mask for the overall land surface area, in order to exclude any non-land components of the MOD11A1 (Land Surface Temperature) and MCD43A3 (Albedo) datasets.

3. Create spatial masks for each vegetation subtype, being careful to exclude any pixels that change land cover type during the 2001-2019 period. The reason for this exclusion is that in this analysis, we wish to understand how surface albedo (and by extension SAF) are changing within a given subtype, and that is different from the effect of changing land cover.

4. Using the spatial masks to exclude non-land and invalid points, we compute a monthly average for LST and albedo, and save the results to netCDF4. For monthly temporal averages, each pixel is treated separately. We sum all of the available daily data, and divide the result by the total number of days. In the equations below k, l are spatial indices, and i is a temporal index. N_{kl} is the number of valid data points in a given month,

$$
\begin{aligned}
\bar{T}_{\text{month},kl} &= \frac{1}{N_{kl}} \sum_{i=1}^{N_{kl}} T_{kl,i} \\
\bar{\alpha}_{\text{month},kl} &= \frac{1}{N_{kl}} \sum_{i=1}^{N_{kl}} \alpha_{kl,i}
\end{aligned}
\tag{2.9}
$$

5. Compute the NET field for each year (2001-2019) with Definition 5 using the monthly averaged fields from the previous step, where $\Delta\alpha_{\text{sfc}}$ is the difference between two months, and ΔT is obtained by taking a spatial average of the difference between monthly averages.

For each year, we have calculated a spatial mean SAF value for each vegetation subtype, performing a spatial integration over each vegetation subtype region Ω_i:

$$
\langle \text{NET}_i(t) \rangle = \frac{1}{A_i} \int_{\Omega_i} \text{NET}(x, y, t) dA
\tag{2.10}
$$

We use these yearly spatial means for each subtype in order to determine the interannual variability in Snow Albedo Feedback for each monthly transition.

2.5 Methodology for Intermodel Comparison

As described in §2.1.2, we performed our analysis on the CMIP6-AMIP model runs. We construct an ensemble of 24 models, and implemented the following methodology.

1. Starting with global input temperature (TS), downwelling radiation (RSDS), upwelling radiation (RSUS), leaf area index (LAI) and vegetation subtype fields, we extract the Arctic sub-regions and mask out Greenland.

2. Reproject all model data to a uniform $1° \times 1°$ grid in order to perform mean and standard deviation calculations over a consistent grid.

3. Given that a uniform lat/lon grid has grid cells that have area that vary with latitude, construct a set of weights w_{ij} to account for this effect (where y_{ij} is the latitude of the ij^{th} grid cell in radians).

$$w_{ij} = \cos(y_{ij}) \tag{2.11}$$

Using Definition 5, we compute the SAF field as a quotient of the upwelling and downwelling radiation fields.

$$\alpha_{\text{sfc}} = \frac{\text{RSUS}}{\text{RSDS}} \tag{2.12}$$

In addition to performing this intermodel comparison, we use the MODIS composites described in the previous section as a reference dataset. We have also computed the zonal means for the original resolutions of each model, and observed only minor ($\leq 0.1 m^2/m^2$) changes to the results compared to the $1°$ grid. This implies that the rescaling procedure does not significantly impact the results, and justifies this approach (of creating a uniform $1°$ ensemble) in the remainder of the analysis.

2.6 Analytic Decomposition of Vegetation Effects

In this section, we introduce an analytic scheme for decomposing the physical effects of vegetation type change from changes within a vegetation type. These methods are applied to our remote sensing analysis of SAF in §3.4.

Our approach relies on a perturbation of the land cover area. We start with a small perturbation to the subdomains Ω_i, and compute its effects on the surface albedo. An

example of such a change in nature would be a subtype composition shift from forest to grassland induced by climate change. As a starting point, we take our expressions for subtype area introduced in §2.3.1.

$$A_i = \text{Area}(\Omega_i) \tag{2.13}$$

We note also that total area is conserved, in keeping with our assumptions specified by the partition framework in §2.2. Using the area fractions γ_i, we note:

$$\gamma_1 + \cdots + \gamma_N = 1$$
$$\sum_{i=1}^{N} \frac{d\gamma_i}{dt} = 0 \tag{2.14}$$

Furthermore, we decompose the albedo into vegetation subtype, and parametrize the albedo climatology of each subtype with M parameters $\vec{x}_i$, with M parameters for each vegetation subtype. Earlier versions of this work used a 4-parameter logistic model, however one of the aims of this decomposition is to show that it is independent of the parametrization scheme.

$$\alpha_i(t) = \alpha(\vec{x}_i, t) \tag{2.15}$$

Next, we consider a model grid cell and perform a subgrid parametrization on the mean albedo $\bar{\alpha}(t)$ as a function of both perturbations. This computation is performed at the subgrid scale, as the MODIS land cover dataset MCD12Q1 is available at the 500m scale, which is much higher resolution than typical ESM grid cells ($\approx$20km). Here, the spatial average is over the model cell, not the entire domain Ω.

$$\langle \alpha(t) \rangle = \int_{\Omega} \alpha(t)dt = \sum_{i=1}^{N} \gamma_i \alpha(\vec{x}_i, t) \tag{2.16}$$

Next, we consider a perturbed $\bar{\alpha}^*(t)$ under the influence of a climatological $\vec{x}_i^* = \vec{x}_i + \Delta \vec{x}_i$ as well as an area perturbation $\gamma_i^* = \gamma_i + \Delta \gamma_i$. The area perturbation reflects a change in vegetation distribution, while the climatological change $\Delta \vec{x}_i$ indicates shifts in the climatology within individual vegetation subtypes.

$$\langle \alpha^*(t) \rangle = \sum_{i=1}^{N} \gamma_i^* \alpha(\vec{x}_i + \Delta\vec{x}_i, t)$$

$$= \sum_{i=1}^{N} (\gamma_i + \Delta\gamma_i) \alpha(\vec{x}_i + \Delta\vec{x}_i) \tag{2.17}$$

$$= \sum_{i=1}^{N} \gamma_i \alpha(\vec{x}_i + \Delta\vec{x}_i) + \sum_{i=1}^{M} \Delta\gamma_i \alpha(\vec{x}_i + \Delta\vec{x}_i)$$

Next, we assume linearity with respect to the perturbed parameters $\vec{x}_i$, and perform the following multivariate Taylor expansion, where the summation index j runs over the M parameters of each vegetation subtype:

$$\langle \alpha^*(t) \rangle = \sum_{i=1}^{N} \gamma_i \Big[\alpha(\vec{A}_i, t) + \sum_{j=1}^{M} \Delta x_{ij} \frac{\partial\alpha}{\partial x_{ij}} \Big] + \sum_{i=1}^{N} \Delta\gamma_i \Big[\alpha(\vec{x}_i, t) + \sum_{j=1}^{M} \Delta x_{ij} \frac{\partial\alpha}{\partial x_{ij}} \Big]$$

$$\langle \alpha^*(t) \rangle = \sum_{i=1}^{N} \gamma_i \alpha(\vec{x}_i, t) + \sum_{i=1}^{N} \sum_{j=1}^{M} \gamma_i \Delta x_{ij} \frac{\partial\alpha}{\partial x_{ij}} + \sum_{i=1}^{N} \Delta\gamma_i \alpha(\vec{x}_i, t) + \sum_{i=1}^{N} \sum_{j=1}^{M} \Delta\gamma_i \Delta x_{ij} \frac{\partial\alpha}{\partial x_{ij}} \tag{2.18}$$

$$\langle \alpha^*(t) \rangle = \bar{\alpha}(t) + \Delta\bar{\alpha}_{\text{clim}}(t) + \Delta\bar{\alpha}_{\text{cover}}(t) + \Delta\bar{\alpha}_{\text{joint}}(t)$$

To add clarity to these terms, we note that the second term $\Delta\bar{\alpha}_{\text{clim}}$ denotes the shift in mean albedo due to shifts in the climatology, $\Delta\bar{\alpha}_{\text{cover}}$ denotes the shift due to land cover changes only, and the final term $\Delta\bar{\alpha}_{\text{joint}}$ is a cross term that contains the joint interaction between the two perturbations.

2.7   Resolution Upscaling Methodology

As a starting point, we take the climatological SAF composites described in §2.4. These pan-Arctic composites are generated in units of $[\% \cdot K^{-1}]$ at the 500m scale. Specifically, we are investigating the NET Snow Albedo Feedback term, as described in Definition 5. In order to investigate the effects of resolution on our ability to resolve SAF, we take the initial $K \times L$ composite of SAF values as our reference matrix $A^{(1)}$. Next, we iteratively upscale our input matrix A^1 by taking block averages.

Example: A single step in the upscaling process for a 4x4 sample matrix. Each increment of the k index for $A^{(k)}$ results in a doubling of the resolution.
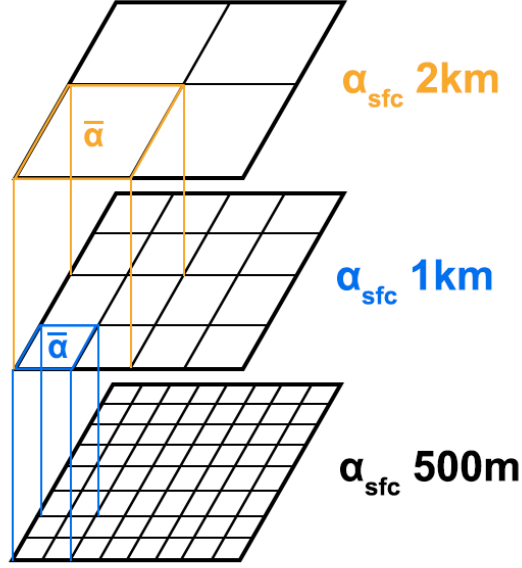
Figure 2.2: Schematic showing the upscaling procedure used in this section as applied to an input albedo grid, starting with a reference resolution of 500m and iteratively doubling the spatial scale.

$$A^{(1)} = \begin{pmatrix} 4 & 3 & 2 & 0 \\ 2 & 1 & 0 & 2 \\ 6 & 2 & 7 & 3 \\ 1 & 3 & 3 & 5 \end{pmatrix} \Rightarrow \begin{pmatrix} 2.5 & 1 \\ 3 & 4.5 \end{pmatrix} \Rightarrow \begin{pmatrix} 2.5 & 2.5 & 1 & 1 \\ 2.5 & 2.5 & 1 & 1 \\ 3 & 3 & 4.5 & 4.5 \\ 3 & 3 & 4.5 & 4.5 \end{pmatrix} = A^{(2)} \qquad (2.19)$$

Through an iterative upscaling process (shown schematically in Fig.2.2), we construct a set of matrices A^k corresponding to upscaled NET fields.. We analyzed iterative doubling of the resolution from 0.5km to 512km. Next, we define the local upscaling error:

Definition 10 *We introduce the **Local Upscaling Error** as the mean normed difference between the original reference matrix (at 500m) and the upscaled matrix. We keep the matrices in the same size (despite the duplicated values that can be seen in Eq.2.19) in order to simplify the calculation of the local upscaling error. Note that each matrix is a $K \times L$ spatial matrix, and that A^k_{ij} denotes a particular pixel of the $A^{(k)}$ matrix.*

$$\Delta A^k = \frac{1}{KL} \sum_{i=1}^{K} \sum_{j=1}^{L} |A^{(1)} - A^{(k)}| \qquad (2.20)$$

26

We note further that this construction satisfies the properties of a matrix norm, as the expression above is equivalent to a matrix norm induced by the L^1 norm and divided by the number of elements in the matrix.

Chapter 3

Characterizing Surface Albedo Variability and Trends Across Scales

The influence of vegetation subtypes on surface albedo has attracted considerable research interest [1] [29] [26] [50]. In this chapter, we use remote sensing data to deepen this analysis. The MODIS dataset at a resolution of 500m provides a long temporal window (2001-2019) at a high resolution, which provides the opportunity to examine land-cover effects that occur at spatial scales that models are not able to fully resolve.

Firstly, we investigate how land cover is changing over decadal timescales, and the resulting changes in surface albedo. Our hypothesis is that these land cover shifts have a detectable influence on SAF over the MODIS data record (2001-2019). Subsequently, we perform climatological analysis of SAF for each vegetation subtype, using the entire spatial domain. The motivation for this analysis is to determine the extent to which vegetation subtype can be used as a predictor of surface albedo, and to examine the temporal and spatial variability within subtypes.

Finally, we investigate the high resolution spatial structure of SAF, in order to test the hypothesis that existing model grid sizes are too coarse to fully capture SAF dynamics. We aim to use this high-resolution dataset to show that performing SAF analysis at model grid scales introduces significant upscaling error, relative to the 500m scale provided by the MODIS remote sensing dataset.

3.1   Land Cover Climatology and Trends

We are interested in vegetation subtype as a predictor of albedo, and to what extent vegetation cover affects the seasonal melt cycle and canopy effects, both of which impact the surface albedo (and by extension, the SAF). We have computed a land cover climatology (2001-2019) over the pan-Arctic domain, showing the percent coverage by land cover type in Fig.3.1. Across the Arctic, land cover is dominated by roughly equal proportions of grass, shrub and needleleaf forest, and small contributions of barren regions and broadleaf forest.
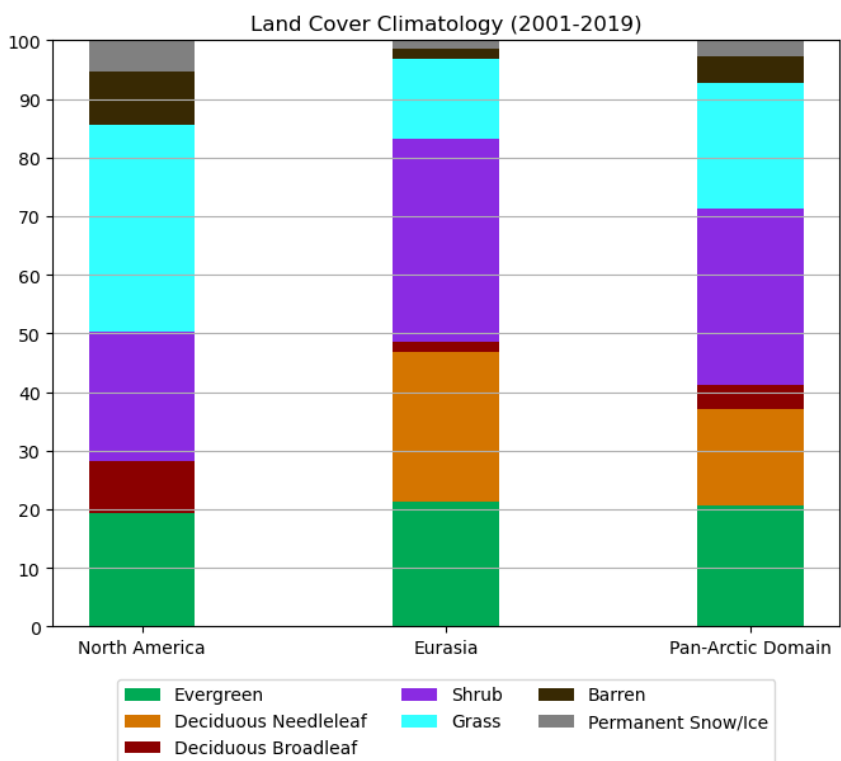
Figure 3.1: Graph showing the relative differences in land cover composition between North America and Eurasia, as well as the full pan-Arctic domain.

The variation between continents is considerable, as North America has more grass (35.3%) compared to the Eurasian grassland cover (13.7%). Additionally, Eurasia has a larger forested percentage due to deciduous needleleaf trees in the larch forests of Siberia. We observe that non-vegetated terrain (barren and permanent snow/ice) represents a much

larger proportion of the domain (9.1% barren, 5.3% permanent snow/ice) in North America, with large sections of the Canadian Arctic Archipelago having barren or glaciated regions. In contrast, the fraction of non-vegetated domain is much smaller over Eurasia (1.7% barren, 1.4% permanent snow/ice), consisting only of a few mountain ranges and far-north archipelagos such as Novaya Zemlya, Severnaya Zemlya and Svalbard. A visualization of the spatial variability in vegetation subtype at the 500m scale is shown in Fig.3.2.

Overall, we can conclude that there are large differences in land cover between continents. This conclusion comes from the MODIS remote sensing dataset, and our resulting analysis of land surface fractions γ_i for each vegetation subtype. We can connect this insight with plant biology - the physical separation of the North American and Eurasian continents has resulted in separate evolutionary pathways for forest species [51] [52]. The intersecting effects of topography and plant evolution have lead to a marked difference in vegetation composition.

In addition to the climatological analysis of land cover, we also perform an interannual analysis to examine trends in vegetation composition (shown in Fig.3.3). For the most part, these vegetation trends are slowly varying in time, with the notable exception of the abrupt drop in deciduous forest cover in Siberia between 2017-2019, which we attribute to wildfire effects. In contrast, we observe increases in deciduous forest area in North America. This shows the large role of local conditions in determining vegetation changes.
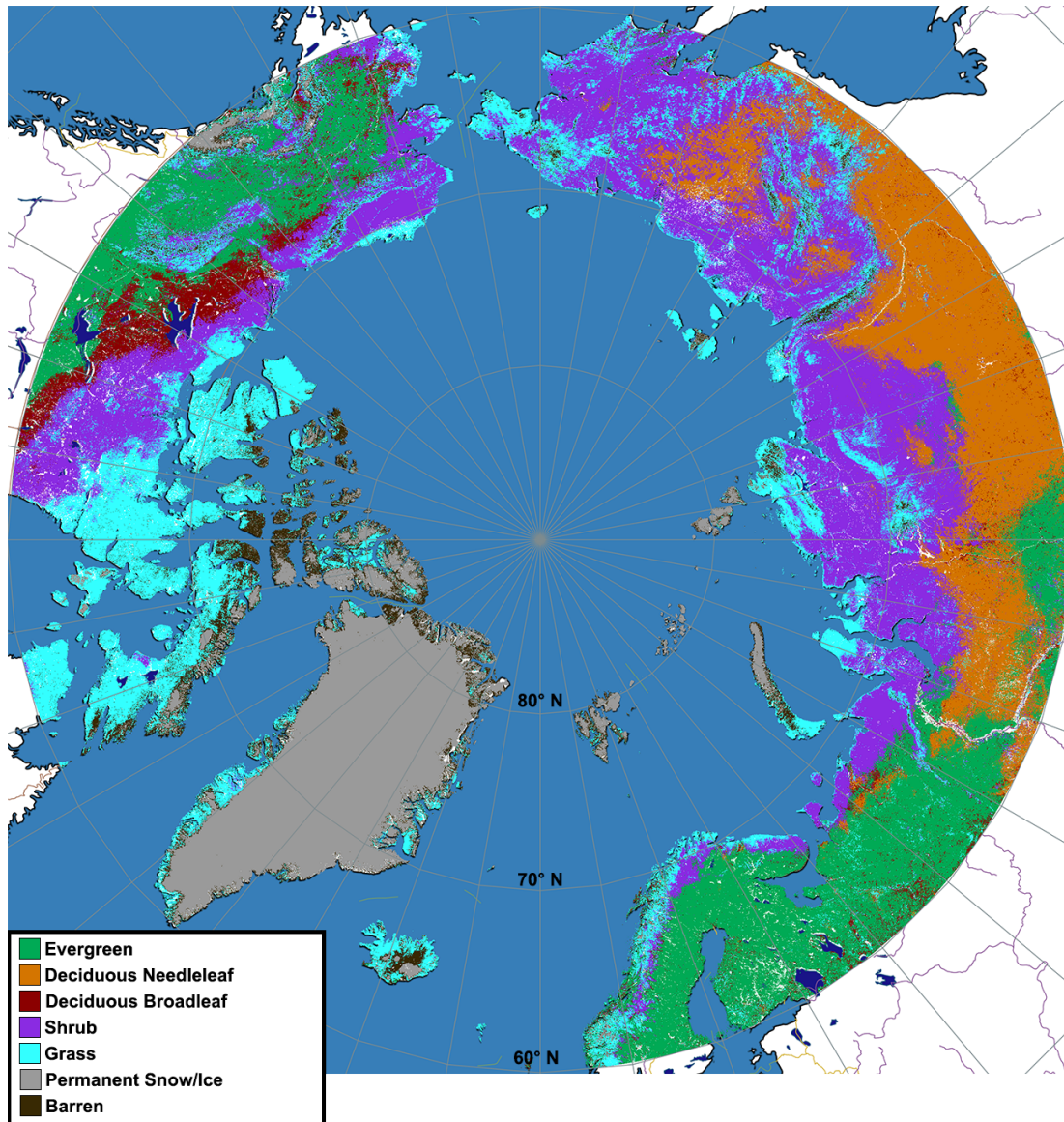
Figure 3.2: This land cover decomposition uses the LC Type 5 classification scheme from the MCD12Q1 dataset at the 500m scale. This analysis reveals complexity in the spatial structure of Arctic vegetation, down to the highest available resolution. We observe fractal patterns in the vegetation, particularly at the interface between vegetation zones. One example of such details is the speckling of deciduous and evergreen forests that we observe in Alaska.

31

Land Cover Changes (2001-2019)
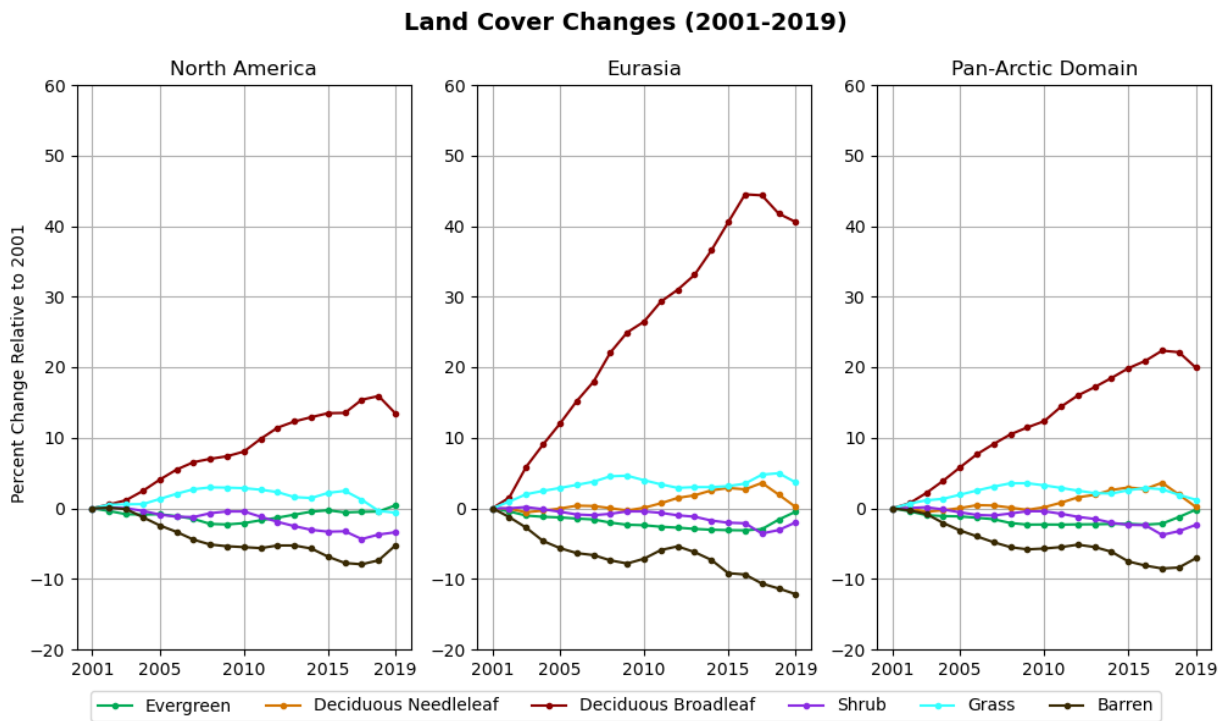
Figure 3.3: Relative change in land cover for each vegetation subtype, compared to 2001 baseline. Deciduous needleleaf has been excluded from the North American plot, given that it covers only 0.034% of the North American land area.

3.2 Albedo Variability within Vegetation Subtypes

In order to investigate the variability within vegetation subtypes, we compute the spatial and temporal variance for each subtype. While the rest of this work uses white-sky albedo (WSA) for consistency with the literature [1], we include the results for black-sky albedo (BSA) for consistency. The results are shown below in Fig.3.4.

In the resulting analysis, we obtain higher values of BSA compared to WSA. This effect is more prominent at earlier times of the year, as well as higher latitudes. This is consistent with the BSA-WSA bias for the Northern Hemisphere shown in the literature [53], and is a function of the solar azimuth angle.

We also note that there is a larger temporal variance during the snow melt period (day 120-200), which corresponds to our intuition that the albedo has more temporal variance during periods of rapid change. Furthermore, we also observe a rise in albedo for barren regions during the month of August, which corresponds to early-onset snowfall due to the combination of high elevation and latitude. Furthermore, we observe a separation in the temporal mean of the three forest types (evergreen, deciduous needleleaf and deciduous broadleaf). This is an effect coming from the influence of plant physiology on the ability of the forest canopy to support snow cover. Based on the work performed in [3], we theorize that evergreen forests must have lower values of either f_{snow} (fraction of canopy covered by snow) or lower values of canopy gap fraction χ compared to deciduous broadleaf forests, with deciduous needleleaf as an intermediate case.

The results for low-height vegetation, as well as barren regions, are consistent with the results from Loranty (2011) [1]. The snow masking effect is much stronger for these vegetation subtypes, as the structure of this vegetation does not provide a snow-free canopy, which results in much higher values of albedo due to snow masking.
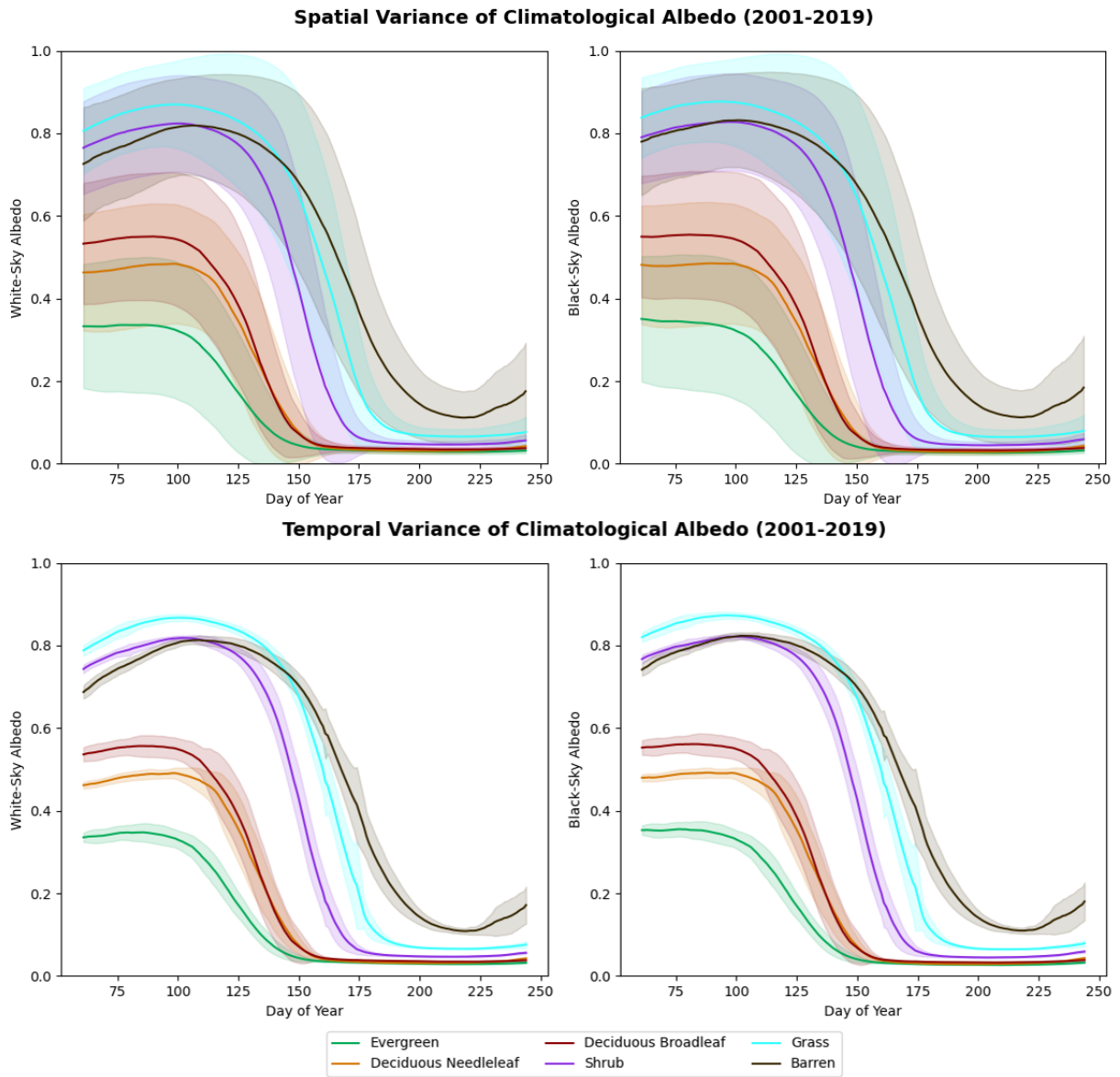
Figure 3.4: Plot showing the spatial and temporal variability of the climatological mean albedo for the pan-Arctic domain for each vegetation subtype. The shaded errorbars on the plot are given by the 1σ contours of the spatial and temporal standard deviation within each subtype.

3.3 SAF Climatology

We have computed a climatology of SAF using the full pan-Arctic domain over the 2001-2019 time period, the results of which are shown in Fig.3.5. We observe that the seasonal cycle of SAF is small for March-April, and peaks in June-July at -2.76 $\% \cdot K^{-1}$. The climatological mean SAF from April-July is $-2.17\% \cdot K^{-1}$. This result is larger than previous results in the literature [54] [55] [56], however this is explained due to differences in methodology. Although some methodological considerations remain fixed (such as the exclusion of Greenland and the definition of SAF as a monthly finite difference), there are several important differences, which we list below.

1. **Spatial Domain:** In our study, we perform an analysis of SAF including all land surface area north of 60°N, while previous studies included a much larger domain. Fernandes et al. (2009) [54] used the Northern Hemisphere APP domain [57], while Fletcher et al. [55] and Thackeray et al. (2016) used a domain including Northern Hemisphere land north of 45°N. Given that the magnitude of SAF generally increases with latitude, we expect our results to have stronger spatial mean SAF, given the absence of low-latitude data points.

2. **Inclusion of additional months:** In our analysis we included an additional month pair, extending the analysis to July/August. We found stronger SAF at high-Arctic latitudes during this monthly transition.

3. **Temporal Domain:** In our analysis we used the temporal domain 2001-2019, while Fernandes et al. studied the observational window 1982-1999. The temporal domain for Fletcher et al. (2015) and Thackeray et al. (2016) was 2000-2004 for observational data. In Fig.3.5 we show that Arctic SAF has an overall negative trend for SAF, which implies that we expect stronger SAF in our more recent period of study.

4. **Observational Data Source:** Fernandes et al. (2009) used the AVHRR (Advanced Very High Resolution Radiometer) APP-x (Polar Pathfinder-x) instrument as the source of albedo data. In contrast Fletcher et al. (2015), Thackeray et al. (2016) and this work used MODIS albedo data.

As part of our analysis, we replicated spatial plots of SAF provided in Fernandes et al. (2009) [54], as well as Fletcher et al. (2015) [55] and performed a qualitative comparison of the NET fields north of 60°N, where the data could be directly compared. In order to make this comparison we restricted the seasonal domain to the months analyzed in previous

studies. We found that the resulting plots were visually consistent with the previous results, indicating that methodological differences were causing the discrepancy.

Additionally, we replicated a zonal plot of NET from Fletcher et al. (2015) [55] and the Hovmöller diagram from Thackeray et al. (2016) and found the distribution of NET values followed a similar pattern. Having performed this analysis we conclude that the results are consistent with the previous literature, after we account for the relevant methodological differences.

In our results for the NET term, we observe a clear negative trend in SAF over the 19-year period of study. Furthermore, the late-season melt-off in June-July has the most negative trend in SAF, with a decrease in SAF of –0.16%/K per decade. Collectively, these results indicate the importance of late-season snow melt to the overall SAF.
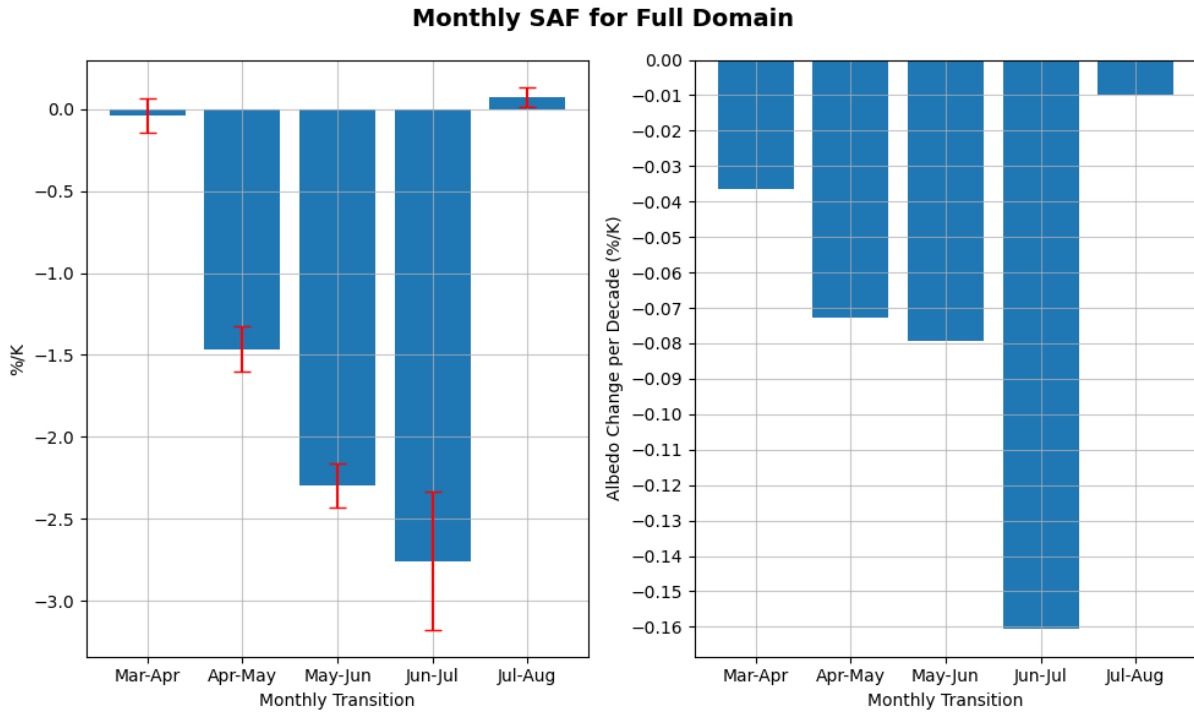
Figure 3.5: Climatological SAF and trend for the temporal period 2001-2019 over the entire domain. The errorbars denote the 1σ temporal standard deviation, representing the interannual variability.

3.3.1 SAF variability by Vegetation Subtype

Using the climatological SAF as a starting point, we further decompose the SAF results by vegetation subtype. Using our partition scheme for vegetation subtype regions Ω_i, we calculate SAF for each year (2001-2019) and each vegetation subtype. The mean, standard deviation and trend for SAF for each vegetation subtype are shown in Fig.3.6.

We observe that barren regions show very high values of SAF (mean $-8.3\% \cdot K^{-1}$ for June-July), as well as an overall negative trend, placing this vegetation subtype as an outlier. Barren regions (4.5% of the pan-Arctic domain) contribute a disproportionate share of the SAF relative to their small spatial extent. Similarly, grassland regions show high SAF for June-July ($-7.2 \% \cdot K^{-1}$). These low-height vegetation classes provide a large contribution to the overall mean SAF.

Given that SAF is calculated from a monthly change in albedo, it is no surprise that the effects observed in §3.2 when we separate albedo into vegetation subtype are replicated for SAF. Specifically, we again observe a separation into the three groups of forested regions (evergreen, deciduous needleleaf, deciduous broadleaf), low-height vegetation (grass and barren) as well as the intermediate case of shrubland. The melt-off over forested regions occurs earlier in the year, leading to SAF peaking during the April-May transition. For grassland and barren regions we observe a melt-off that occurs much later in the season during the June-July transition.

Overall, we observe that the trends are essentially flat for the early-season melt period. We note that these trends are linearizations, and they are plotted on top of considerable interannual variability in SAF. One noticeable outlier is deciduous forest, which shows a positive SAF trend for the monthly transition of May-June. The increase in the magnitude of SAF is primarily driven by the strongly negative trends of grassland and barren regions. Given the spatial distribution of vegetation shown in Fig.3.2, this implies high-Arctic regions are highly significant in driving increases in the strength of the SAF.

3.3.2 Spatial variability in SAF

A visualization of the climatological SAF composites is shown in Fig.3.7. Generally, the spatial distribution of the MODIS results and the intermodel mean agree, however there is a discrepancy for the late-season melt-off. In particular, high-Arctic barren and grassland regions show much higher results in the MODIS SAF climatology compared to the AMIP intermodel mean.
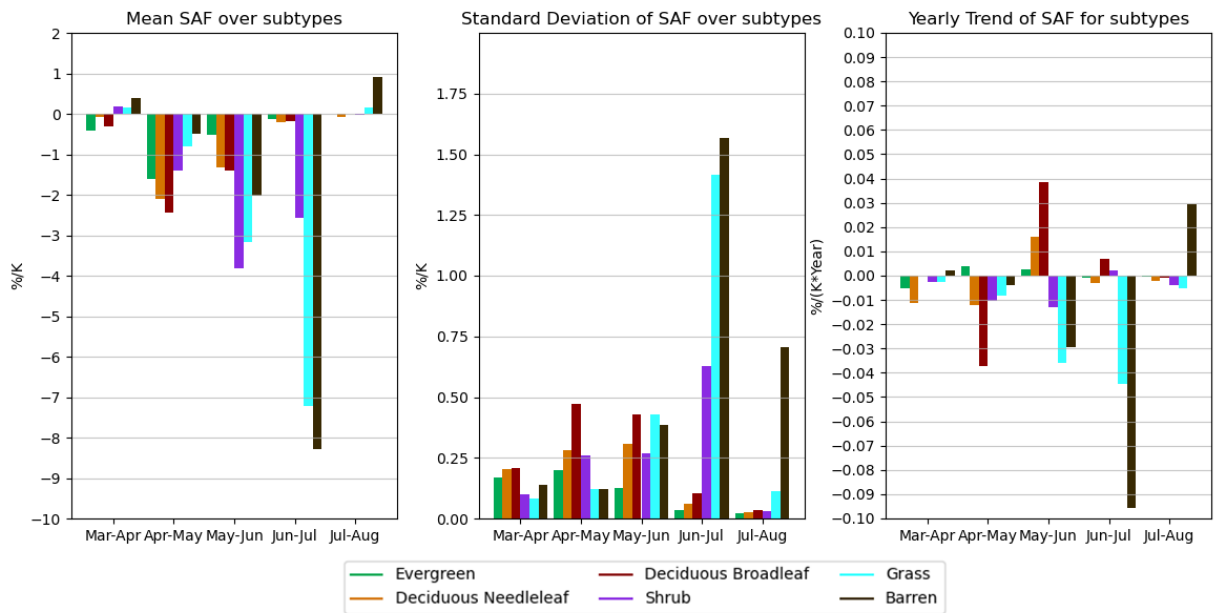
Figure 3.6: Mean SAF for each vegetation subtype. We observe very strongly negative values of SAF for grass and barren regions, with shrubs as an intermediate case between forested and grassland regions. SAF standard deviation, computed over the results from 2001-2019. We observe a clear separation in the May-June and June-July transitions, with grass and barren regions showing a much larger standard deviation. SAF trends by subtype, showing very different behavior depending on which vegetation subtype.

By going to the 500m scale, we observe large values of SAF for the grass and barren regions during the June-July transition. These SAF values (in some cases as low as -16 %/K) are well outside of the range established by previous results. Our hypothesis for these extremely high values of SAF for the grass and barren subtype is the greater efficiency that additional heating has on creating a melt-off transition for low-height vegetation compared to forested regions. These values of SAF indicate a particularly strong SAF forcing for these vegetation subtypes, as well as a need for high-resolution analysis to fully capture these regions.

By using grid sizes that are too large to resolve this gradient, we introduce errors into our analysis of SAF, which will be explored in more detail in §3.5.
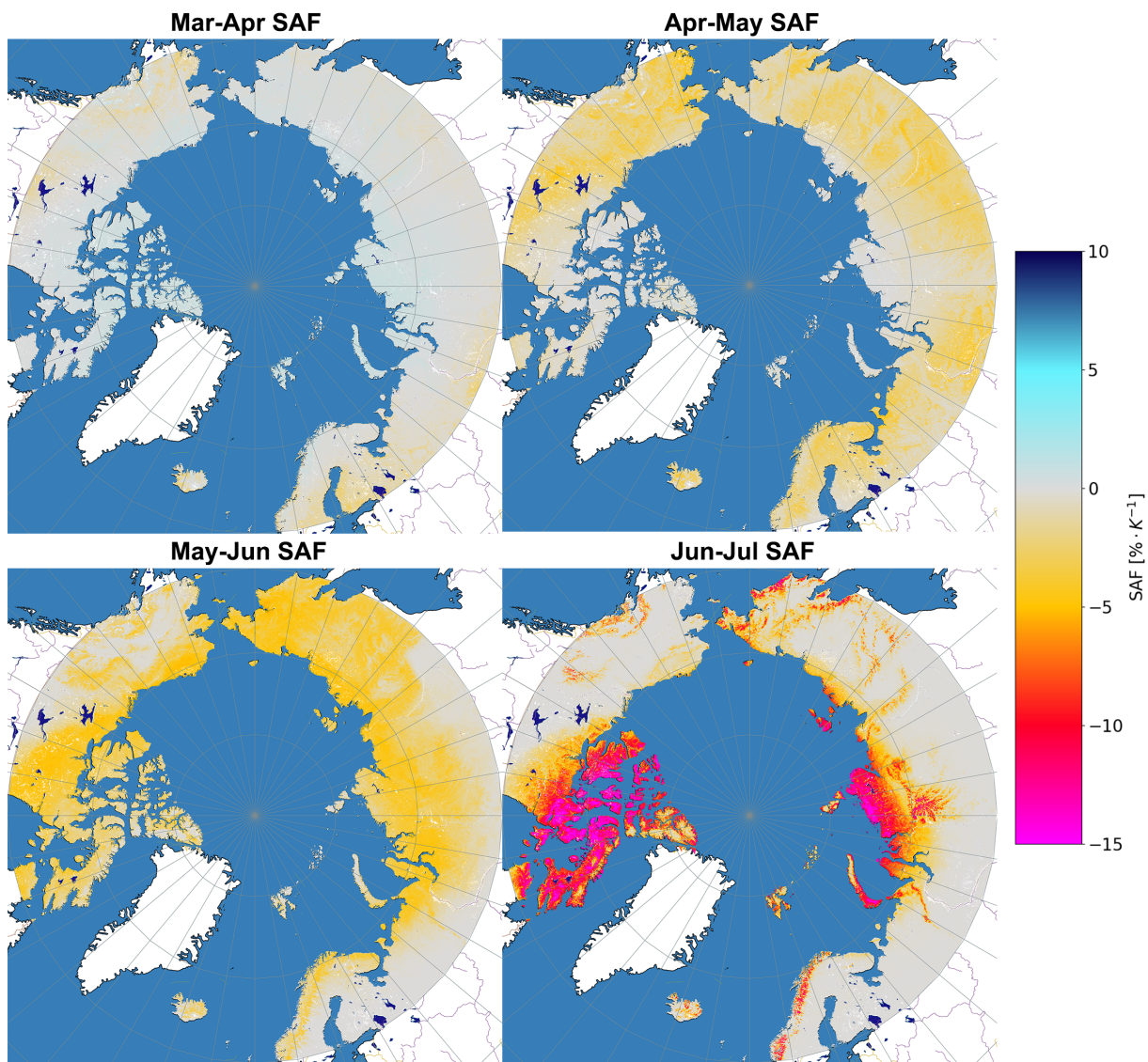
Figure 3.7: Climatological NET SAF from 2001-2019 over the pan-Arctic domain.

3.4 Decomposition of SAF Changes

3.4.1 Analytic Derivation

In this section, we extend the analytic decomposition developed in §2.5 for albedo, and apply it to SAF directly. We wish to separate the effects of land cover changes from shifts in climatology, and use this framework to perform a retrospective analysis of SAF changes from 2001-2019.

Consider our domain Ω, as well as the partitions into M subdomains Ω_i according to vegetation subtype. In this work, we use the MCD12Q1 Land Cover Type dataset. Additionally, must consider that land cover types change on a yearly basis (as this is a yearly product), so we add an additional temporal index t to denote the year. The index set $t \in [1, 19]$ corresponds to the years $[2001, \cdots, 2019]$ for our dataset.

Taking the spatial average of the NET term of the snow albedo feedback, we use the Eq.2.6 over the domain Ω, where dA is an area element.

$$\langle \text{NET}_t \rangle = \int_\Omega \text{NET}_t(x, y) dA \tag{3.1}$$

As we are interested in the mean, we split the integral over each subtype (not necessarily contiguous), and take the following approximation, taking the average for each subtype:

$$\begin{aligned}
\langle \text{NET}_t \rangle &= \sum_i^M \int_{\Omega_i} \text{NET}_t(x, y) dA \\
&\approx \sum_{i=1}^M \gamma_{i,t} \langle \text{NET}_{i,t} \rangle
\end{aligned} \tag{3.2}$$

With this expression for the spatial mean of the NET term, we consider a perturbation of the land surface area as well as the subtype mean NET:

$$\begin{aligned}
\gamma_i^* &= \gamma_i + \Delta\gamma_i \\
\text{NET}_i^* &= \text{NET}_i + \Delta\text{NET}_i
\end{aligned} \tag{3.3}$$

This allows us to explicitly construct the change in NET due to land cover changes $\Delta\text{NET}_{\text{cover}}$, changes due to climatological shifts $\Delta\text{NET}_{\text{clim}}$ as well as the joint interaction $\Delta\text{NET}_{\text{joint}}$. For the next set of equations, all of these deltas are assumed to be spatial averages, and we drop the angle brackets for simplicity.

41

$$\Delta\text{NET}_{\text{cover}} = \sum_{i=1}^{N} \Delta\gamma_i \text{NET}_i$$

$$\Delta\text{NET}_{\text{clim}} = \sum_{i=1}^{N} \gamma_i \Delta\text{NET}_i \tag{3.4}$$

$$\Delta\text{NET}_{\text{joint}} = \sum_{i=1}^{N} \Delta\gamma_i \Delta\text{NET}_i$$

Using the analytic decomposition from the previous subsection, our goal is to decompose the change in NET from 2001 to 2019 over vegetated regions. We combine the results from §3.1 for land cover changes γ_i with the linearized SAF trends shown in Fig.3.6 to compute the decomposition shown in Eq.3.4. The results of this decomposition are shown in Fig.3.8.

Our original hypothesis was that land cover changes have a significant impact on vegetation. We find that these land cover changes have a small but nonzero contribution to the overall SAF, particularly in the May-July months. We find that for the May-June transition, $\Delta\text{NET}_{\text{cover}}$ contributed 8.0% of the total change in NET, and over the June-July transition the percentage of SAF change caused by land cover effects was 10.1%.
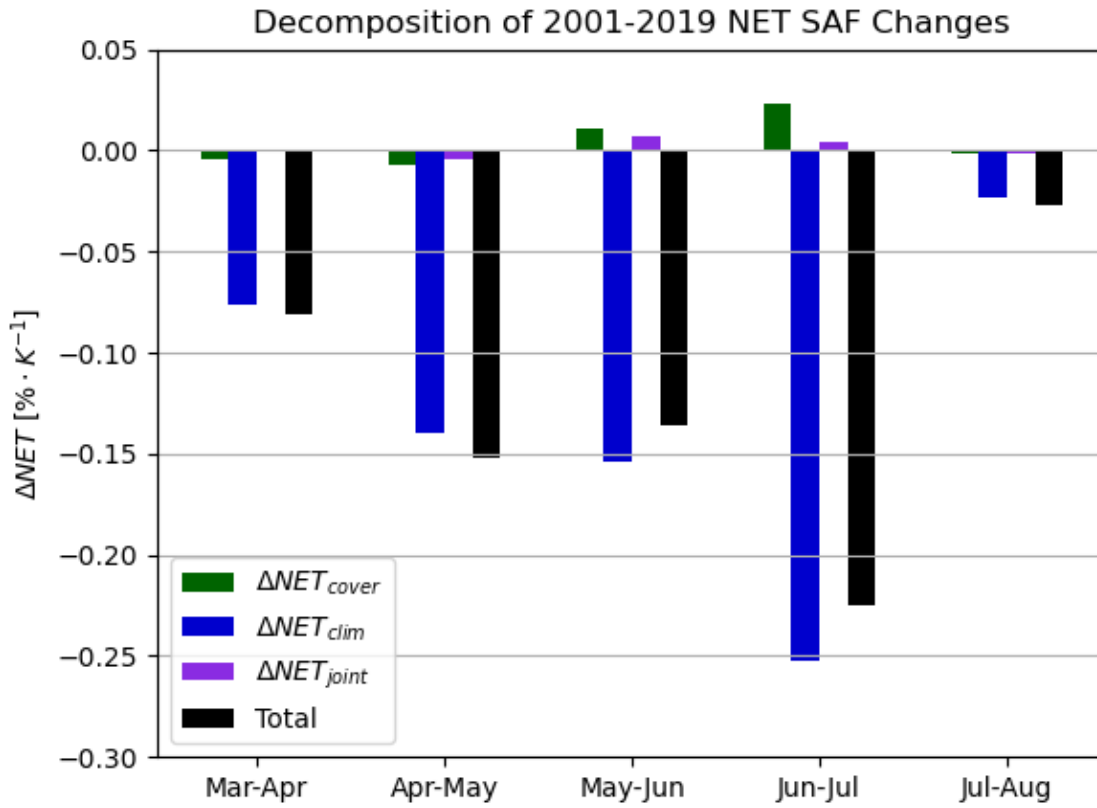
Figure 3.8: This plot shows the decomposition of the mean change in SAF between 2001-2019 averaged over the subtypes of deciduous forest, evergreen forest, shrub, grass and barren regions. We observe negligible effects due to land cover changes (i.e. a change in vegetation subtype) until the May-July months, at which point it becomes a significant contributor. Interestingly, land cover changes have a net damping effect on the snow albedo feedback during these months, leading to a cooling effect that reduces the strength of the SAF.

3.5   Effects of Resolution on SAF Errors

We have two related questions:

1. What are the spatial scales of variability in SAF?

2. What is the influence of resolution on local and global errors in SAF?

The use of high-resolution snow and vegetation data involves considerable computational overhead at the 500m and 1km level. Therefore, we wish to first demonstrate that making use of these datasets at the maximum resolution provides significant benefits in terms of an ability to reconstruct surface albedo α_{sfc} as well as the SAF (Snow Albedo Feedback).

Having computed a series of monthly composites for climatological SAF, we aim to degrade the resolution of these fields to observe the local upscaling error, as defined in 10. By starting at the 500m scale, and iteratively doubling the size of the grid up to 512km, we observe the resulting impacts on SAF accuracy.

After computing the local upscaling error $\Delta\text{NET}^{(k)}$ for each monthly transition between February and July, the results can be seen in Fig.3.9. We observe a very sharp increase in error between the spatial scales of 500m and 100km. In contrast, the larger spatial scales contribute much less overall to the error. We also note that the June-July monthly transition appears as an outlier, showing a much higher degree of spatial variability at all spatial scales compared to other monthly transitions.

We have defined an analogous local upscaling error for the input albedo fields α_{sfc}, which resulted in similar error scaling. Given that the definition of the NET term involves a spatial average of surface temperature over the entire pan-Arctic domain, upscaling the temperature field will not impact the NET term. Thus we can conclude that high-resolution spatial heterogeneity in the albedo field yields the same heterogeneity in the reconstructed SAF NET field.

The need for high-resolution analysis of SAF can be thought of as the combination of two effects. Firstly, complex coastline topography requires high spatial resolution in order to properly separate land pixels from water. A good example of this is the Canadian Arctic Archipelago. Secondly, within the land regions we can have high spatial heterogeneity of SAF within a small spatial extent.
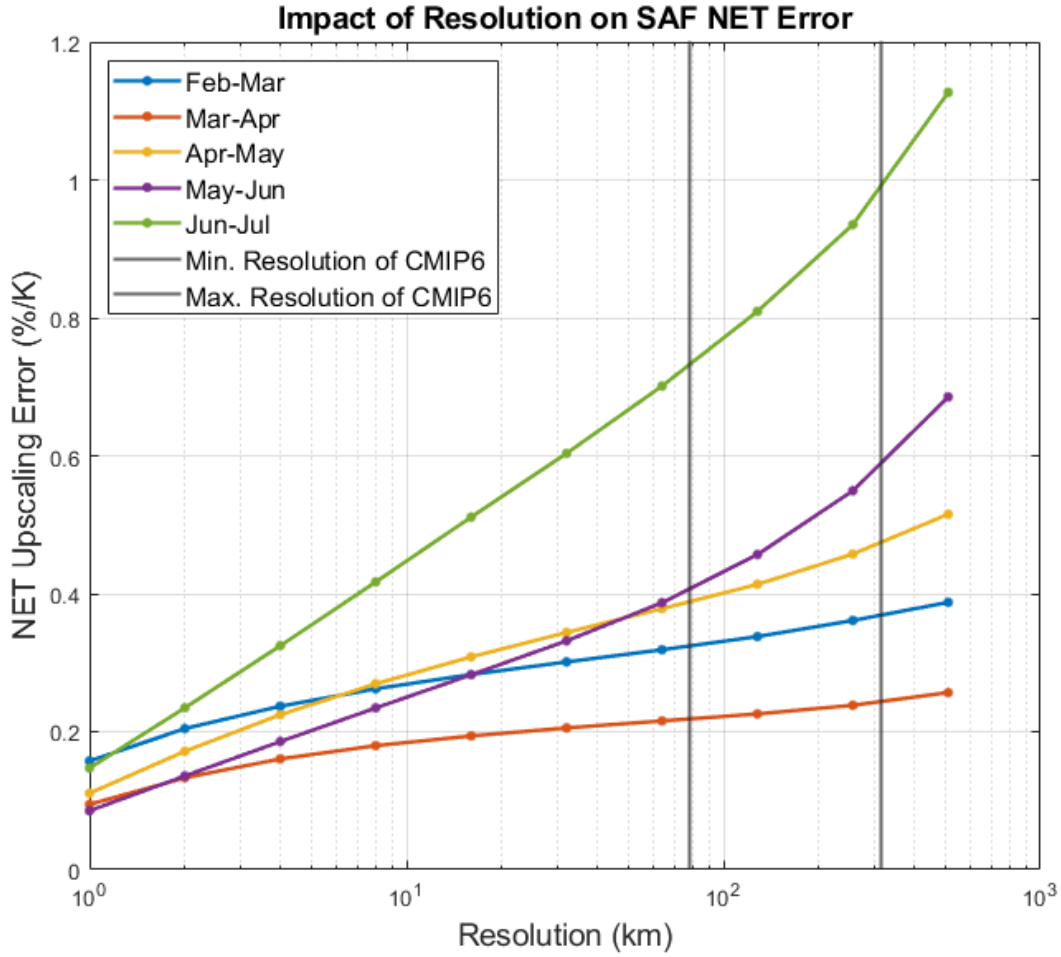
Figure 3.9: Local upscaling error for the NET SAF component as a function of grid resolution.

3.5.1 Influence of Resolution on Global SAF Error

Having established a high degree of spatial variability at grid sizes smaller than model cells (≈100km), we wish to calculate the impact of local upscaling error on global error in SAF. That is, to what extent do these high-resolution local errors contribute to bias in the pan-Arctic estimate for SAF?

Given that June-July are the months where the spatial variability in SAF is largest, we

perform a spatial visualization of the local upscaling error in Fig.3.10. First we compute SAF at the 500m scale, then degrade the resolution of the input albedo fields to 100km and perform the SAF calculation at the model grid scale. We observe a mean absolute local error of $0.773\% \cdot K^{-1}$ over the entire domain.

However despite these large local errors, this does not translate into a significant bias in the pan-Arctic estimate for SAF. The results for the 500m and 100km SAF fields are quite similar, with only a 2.23% (relative) change in the overall result.

$$< SAF_{500m} >= -2.617\% \cdot K^{-1} \tag{3.5}$$

$$< SAF_{100km} >= -2.559\% \cdot K^{-1} \tag{3.6}$$

Despite the 100km grid failing to capture the high-resolution dynamics, these local errors largely cancel each other out, resulting in a only a small global error $\Delta SAF = 0.058\% \cdot K^{-1}$. We have demonstrated the existence of high-resolution spatial structure in SAF, however we cannot conclude that resolution is a driving factor behind the intermodel spread in SAF.

Our original hypothesis predicted that vegetation subtype was the primary source of spatial variability in SAF. However, when comparing Fig.3.2 and Fig.3.10, we observe that many areas of high variability are found in mountainous regions with sharp elevation differences, such as the Arctic Cordillera and the Scandinavian Mountains. This indicates that topography also plays a role in high-resolution SAF features.
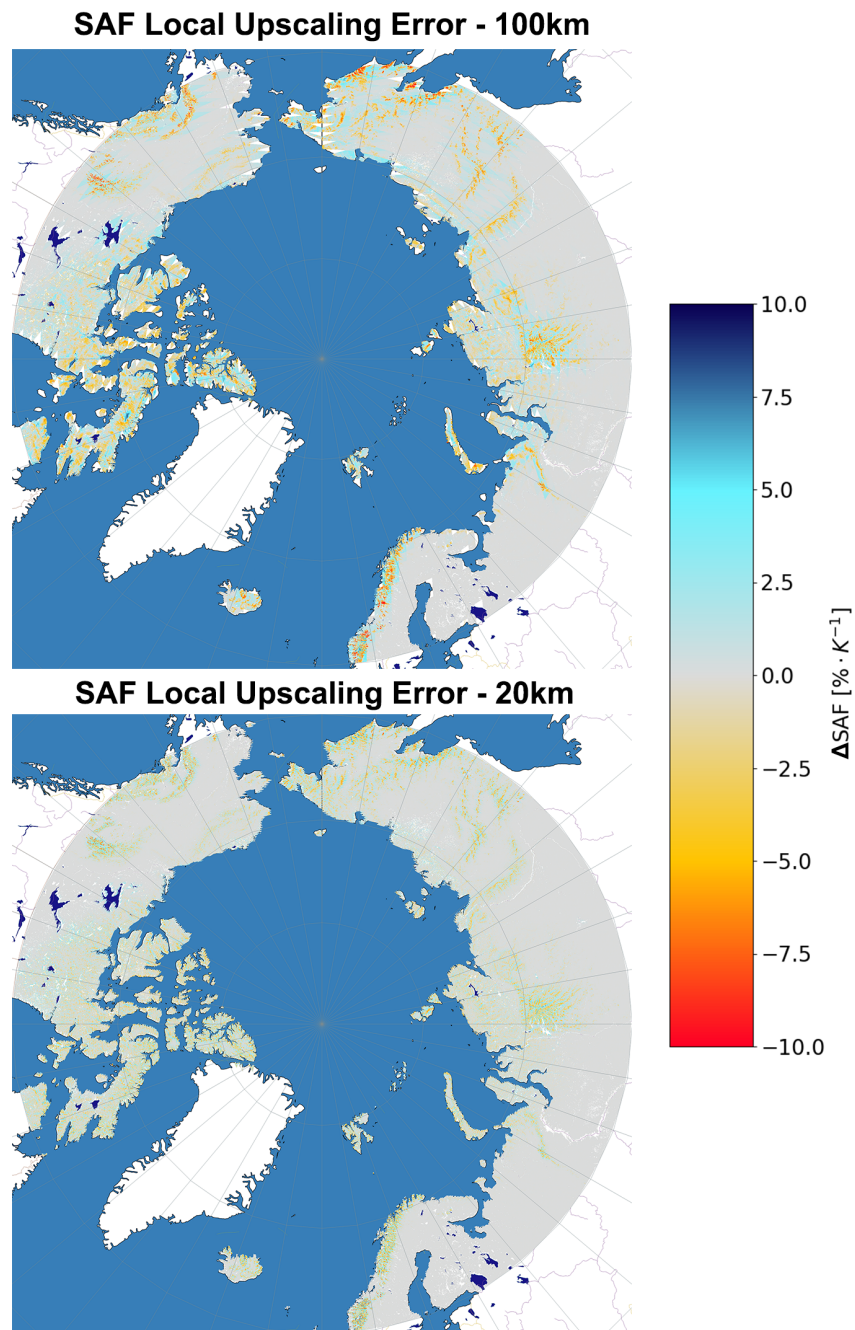
Figure 3.10: Spatial plot of local upscaling error for June-July. Indicates difference between 500m and upscaled results, with values in red corresponding to a stronger SAF at the 500m scale.

Chapter 4

The Role of Vegetation in SAF Intermodel Spread

Using the CMIP6 AMIP (Atmospheric Model Intercomparison Project) data described in §2.1.2, we use the methodology described in §2.5 to generate an ensemble of 24 models. This explores the link between vegetation properties and SAF, with a particular focus on Leaf Area Index (LAI). First, we perform an analysis of LAI spread within the CMIP6 ensemble, and compare the results to MODIS observational data. We perform a similar intermodel comparison to examine model SAF spread. Finally, we use both datasets to show that SAF has a logarithmic dependence on LAI. We fit logarithmic curves to the LAI/SAF relationship for each model, and find considerable intermodel spread in the values of the fit parameters.

4.1   Analysis of LAI for the CMIP6 Ensemble

LAI is a key determinant of albedo, as shown in [3] for the CMIP5 ensemble. In this work, Wang et al. demonstrated that albedo has high sensitivity to LAI biases, particularly for low values of LAI. The analytic results were specific to the CLASS (Canadian Land Surface Scheme) model, however this paper also demonstrated the link between LAI biases and albedo bias for other models in the CMIP5 ensemble. We aim to further deepen this investigation by updating the results for CMIP6, and extending the analysis to include the link between LAI and SAF.

In Fig.4.1, we have performed a zonal comparison of LAI for each of 24 members of the CMIP6 ensemble, as well as the MODIS observational dataset. We observe that model LAI
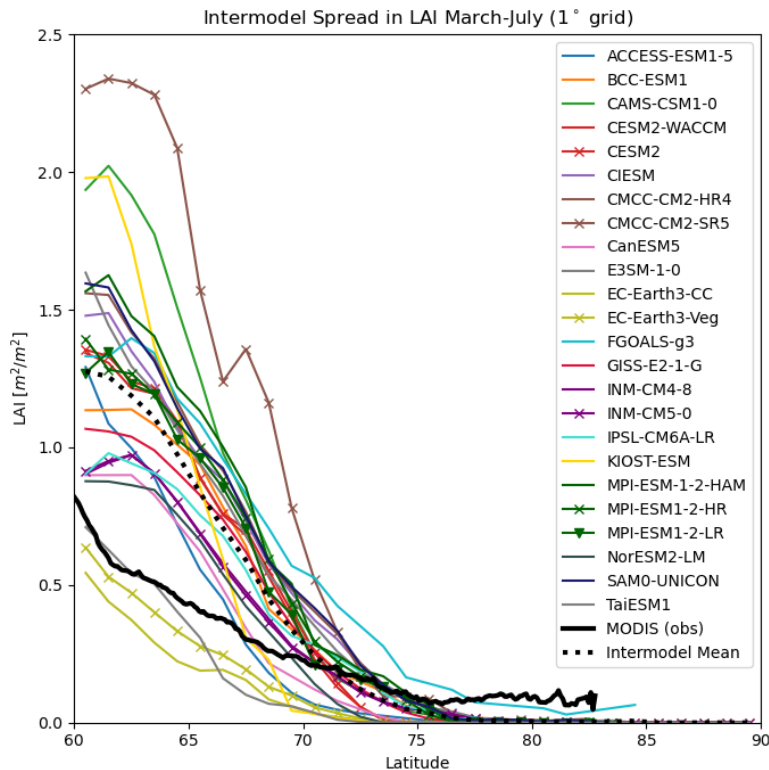
Figure 4.1: Comparison of LAI spread within the AMIP ensemble.

north of 70° is consistent with MODIS results, while the intermodel mean is considerably higher than MODIS results between 60N and 70N. This latitude band contains large regions of boreal forest (as shown in Fig.3.2). This diagnostic implies that there is considerable spread in how different models represent these forested regions.

The fact that MODIS observations show lower LAI values over forested regions than the intermodel mean is consistent with recent results [58] showing MODIS LAI has considerably lower values of LAI compared to ground measurements. The impact of models having higher LAI is a corresponding decrease in albedo, particularly earlier in the melt season (Feb-Apr). We conclude this based on our results in Fig.3.4 showing lower albedo for forest subtypes compared to vegetation-free regions. This is consistent with [3] demonstrating that increased LAI leads to decreased surface albedo.

4.1.1 Multi-model Mean and Intermodel Spread

In Fig.4.2 we have performed a seasonal climatology of LAI, showing the mean and standard deviation over the entire spatial domain, from 2001-2014. We observe that the regions covered by evergreen needleleaf, particularly Scandinavia/Russia west of the Ural mountains show large spread year-round. Additionally, in July there exists large disagreement not only in evergreen forest regions but in Siberian shrub/grassland regions.

Within the 24-member AMIP ensemble, we have a few notable outliers such as EC-Earth-CC, EC-Earth-Veg and CMCC-CM2-SR5. In this section, we explain the behavior of the outlier models using the vegetation datasets. In this section, we perform an analysis using LAI and vegetation subtype on 3 models: ACCESS-ESM1-5, CMCC-CM2-SR5 and EC-Earth3-CC. We are limited to an analysis of these models due to the availability of vegetation subtype data, shown in Table 2.2. Leaf Area Index (LAI) and vegetation subtype can both be used as predictors of albedo, however they are not completely independent quantities.

In order to investigate how different CMIP6 models represent vegetation subtype, we have first performed a land cover climatology in Fig.4.4, excluding glaciers and bodies of water. We observe that the CMCC-CM2-SR5 model is close to the MODIS dataset, however the ACCESS-ESM1-5 model combines grassland and shrub into a single category. In the case of the EC-Earth3-CC model [59], we see considerable disagreement with observational data, as 88% of the domain is represented as barren, as shown in Fig.4.1. The reason for this discrepancy is that vegetation is used as a tunable parameter in ESM model development, as vegetation provides a key control on surface albedo [26].
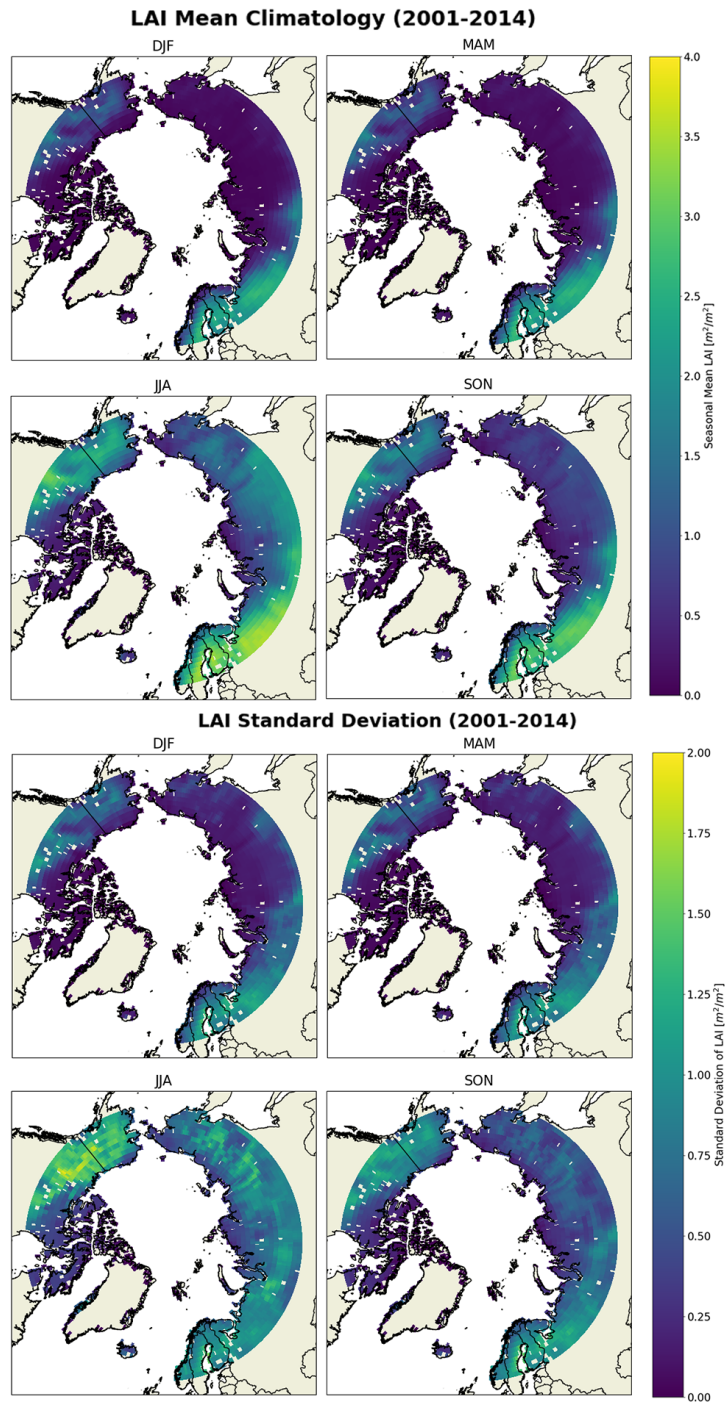
Figure 4.2: Spatial representation of seasonal mean and standard deviation for LAI, where the standard deviation is taken for N=24 models for each point in the domain.

Mar-Jul Seasonal Average LAI
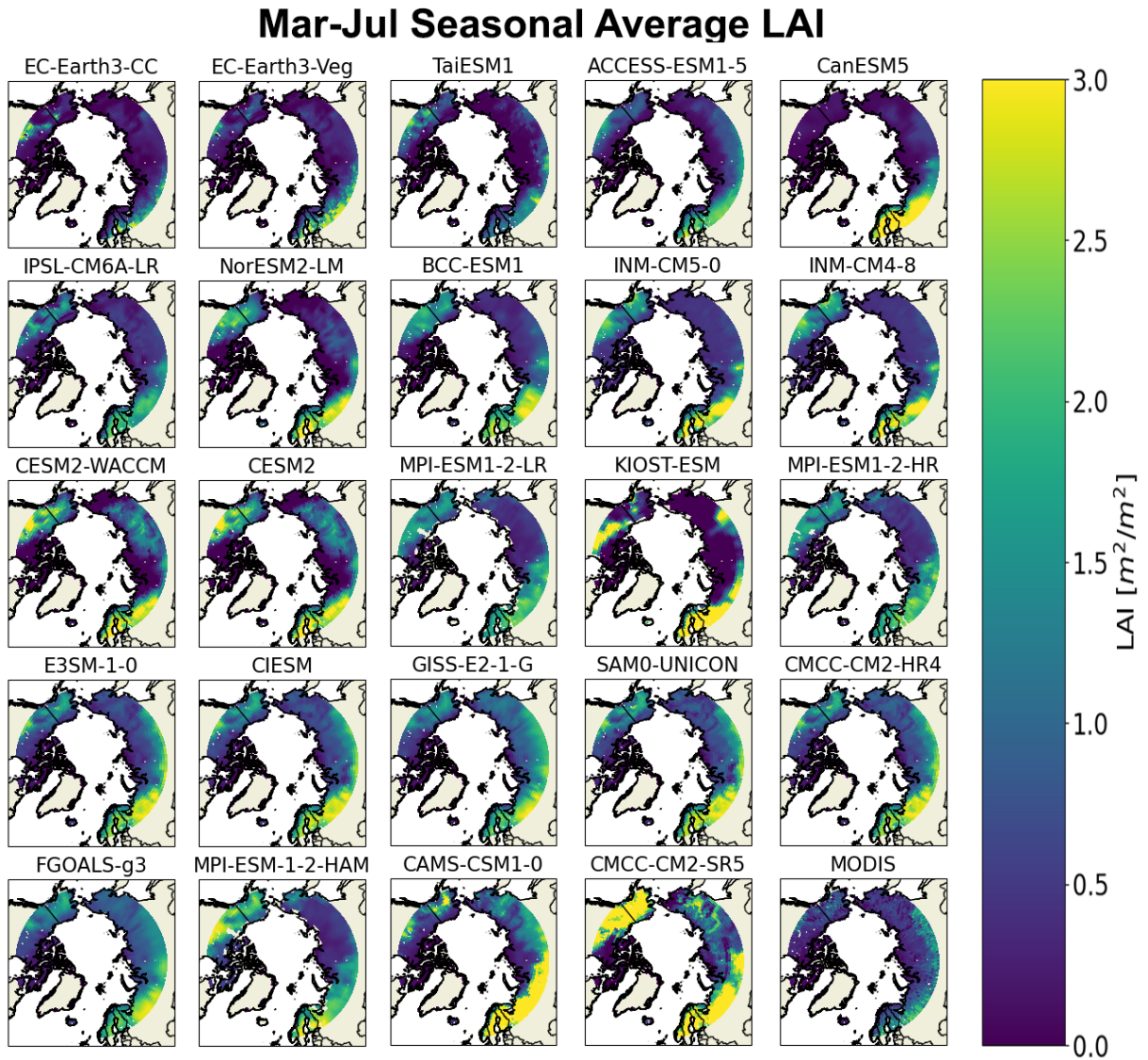
Figure 4.3: Grid plot showing March-July LAI climatology from 2001-2014 for the 24 ensemble members, as well as MODIS remote sensing data.
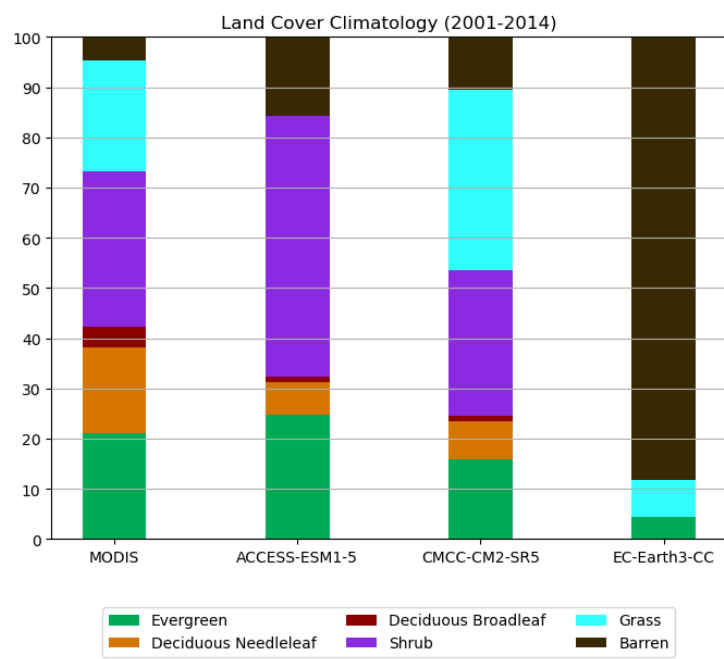
Figure 4.4: Land cover climatology for 2001-2014

4.2 SAF Results for CMIP6 Ensemble

A clear difference between MODIS observational and the AMIP experiments is the strength of the Snow Albedo Feedback, particularly during the June-July transition. The MODIS observations indicate consistently stronger SAF values than predicted over the months June-July, shown in Fig.4.5. This implies that existing models underestimate the surface radiative heating caused by the Snow Albedo Feedback, as a stronger SAF will produce increased warming.

For the Feb-March transition, the intermodel mean shows unphysical values of SAF, which is due to the behavior of the EC-Earth3-CC and EC-Earth3-Veg models. For this reason, we exclude these models from our ensemble analysis of SAF. We explore this in further detail in the case studies in §4.2. Furthermore, we perform a spatial standard deviation of the SAF results in Fig.4.6. We find the areas where the models disagree the most correspond to the MODIS barren/grassland types. This indicates a need for a more careful approach to parametrizing radiative feedbacks in these high-Arctic subtype regions.
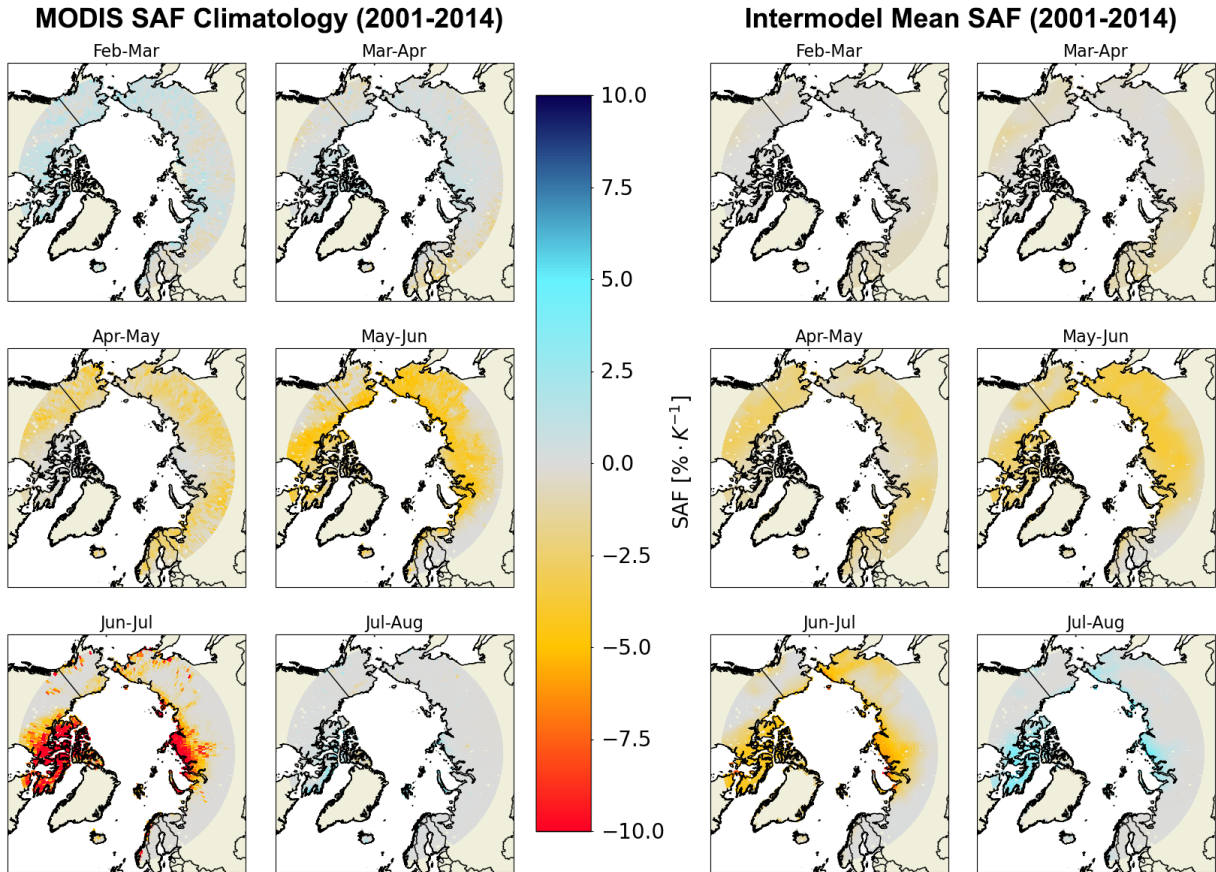
Figure 4.5: Comparison of observational (MODIS) and model ensemble SAF climatologies. Note that both EC-Earth3-Veg and EC-Earth3-CC have been excluded from the ensemble due to unrealistic values of temperature.
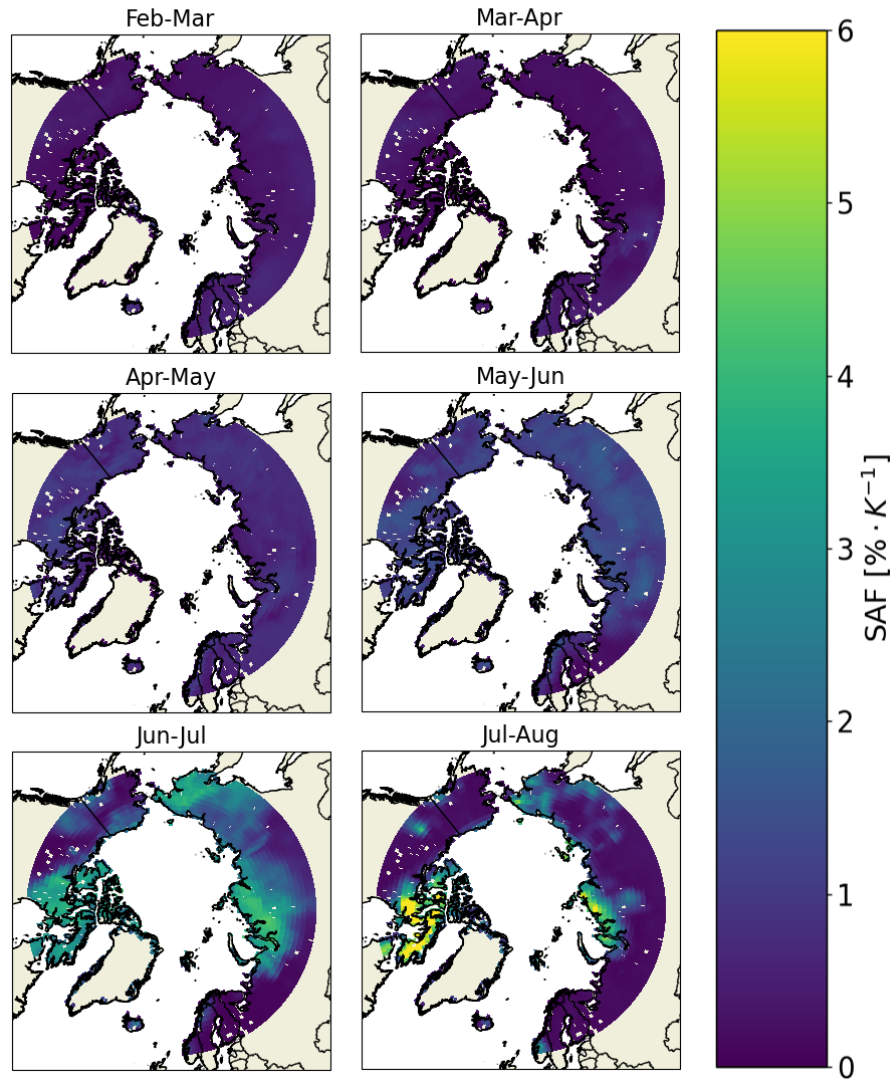
Figure 4.6: Intermodel standard deviation of 2001-2014 SAF climatology.

4.3 Link Between Variability in LAI and SAF

4.3.1 Intersection Between Vegetation and Surface Characteristics

Wang et al. (2016) [3] performed an analysis of the seasonal cycle of albedo and LAI for the CMIP5 ensemble over a subdomain of Eurasia. We repeated this analysis (not shown) for CMIP6 and observed the spread of LAI and Albedo are comparable, showing similar ranges for CMIP5 and CMIP6. This indicates that intermodel spread in LAI and albedo is an ongoing issue for the current generation of climate models. Subsequently, we extended this analysis ot the entire pan-Arctic domain for the 24 CMIP6 models in our ensemble, and included SAF and surface temperature as well, the results of which are shown in Fig.4.7.

The results from this analysis are consistent with the spatial plots in Fig.4.5, in that there is a clear discrepancy in SAF between MODIS observational results and the intermodel mean for the June-July transition, with observational results showing higher values of SAF than the intermodel mean during this period. Additionally, we observe a significant discrepancy in early-season LAI values for MODIS and model data. We note that the MODIS mean LAI for Feb-April is 0.083, while the intermodel mean for the same period is 0.537.

The Earth3 models are clear outliers in terms of representation of vegetation. Combined with the vegetation subtype analysis that shows the EC-Earth3-CC model as 88% covered by barren regions, we can conclude that these models severely underestimate LAI. Another outlier is the CMCC-CM2-SR5 model, which shows very high values of SAF over forested regions, which is not consistent with either the MODIS observational data or the intermodel mean.

In addition to being an outlier for vegetation, the EC-Earth3-CC model (as well as EC-Earth3-Veg) are outliers for representing Arctic temperatures. While other models show a monthly temperature increase between $5 - 7°C$ for the Feb-Mar transition, the EC-Earth3-CC model has a monthly delta of only $\Delta T = 0.013°C$ for these months. Given that the temperature difference is the denominator in Definition 5, this yields nonphysical results for NET during these months.

We observe that the monthly temperature differences (shown in Table 4.1) in the MODIS dataset are inconsistent with the intermodel mean, while the data provided by Berkeley Earth shows good agreement. Previous validation work [60] has shown MODIS overestimates daytime LST. Given that the ΔT values are larger for MODIS, this implies

Monthly ΔT	Feb-Mar	Mar-Apr	Apr-May	May-Jun	Jun-Jul	Jul-Aug
MODIS	8.84	10.50	12.37	13.48	4.13	-4.46
Berkeley	6.59	9.58	10.21	8.57	3.59	-2.76

Table 4.1: Monthly temperature differences, comparing the two observational datasets (MODIS and Berkeley Earth).

our results may be underestimating SAF (since ΔT appears in the denominator). However, this does not change our conclusion that observations show stronger SAF than the intermodel mean.

4.3.2   Empirical Model of the LAI-SAF Relationship

For this analysis, we take the maximum annual SAF at each grid cell. We plot the resulting distribution of points (for all models combined) in a histogram shown in Fig.4.8. We observe that there are no regions with high LAI that show strong SAF values. This implies that vegetation cover is protective against high SAF values. There is a straightforward interpretation of this result in terms of canopy effects - as shown in Fig.3.4, we note the albedo contrast between $\alpha_{\max}$ and $\alpha_{\min}$ over the seasonal cycle is much smaller for forested regions than for low-height vegetation.

Given that the numerator of the NET term of the Snow Albedo Feedback is a monthly albedo difference, this places a hard limit on the maximum strength of the SAF for forested regions, since the maximum SAF for a given grid point is bounded by the following expression:

$$\text{NET} \leq \frac{\alpha_{\min} - \alpha_{\max}}{<\Delta T>} \tag{4.1}$$

Subsequently, we have used the maximum SAF values from the CMIP6 AMIP ensemble and fit curves to each model individually. We fit these data points to logarithmic curve with two fit parameters (shown in Eq.4.2), excluding values with LAI ≤ 0.1 to avoid singular values close to zero. Based on these results shown in Fig.4.10, we conclude that the strength of SAF decreases as a function of LAI, and that the relationship is well captured by a logarithmic curve. This is consistent with results in [14] showing saturation effects in the LAI-albedo relationship. The physical interpretation of this response curve is that forested regions have a smaller difference between minimum and maximum albedo due to canopy masking, which implies a constraint on the maximum NET as shown in Eq.4.1.
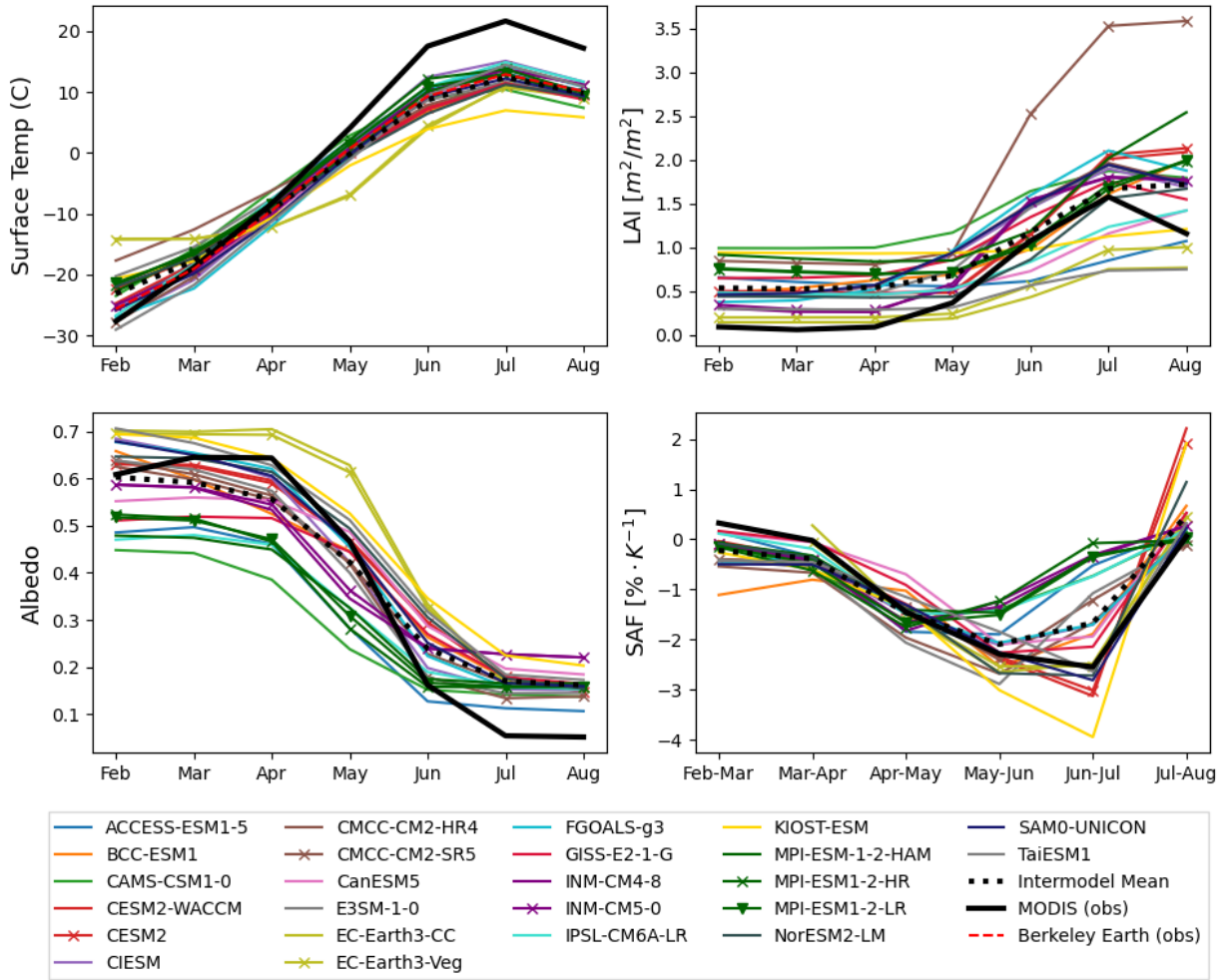
Figure 4.7: Extension of [3] for the entire spatial domain north of 60N, from 2001-2014. The EC-Earth3 SAF results are omitted for Feb-Mar due to the singular behavior caused by the unexpectedly small temperature difference $\Delta T = 0.013°C$ that EC-Earth3 models show for these months.
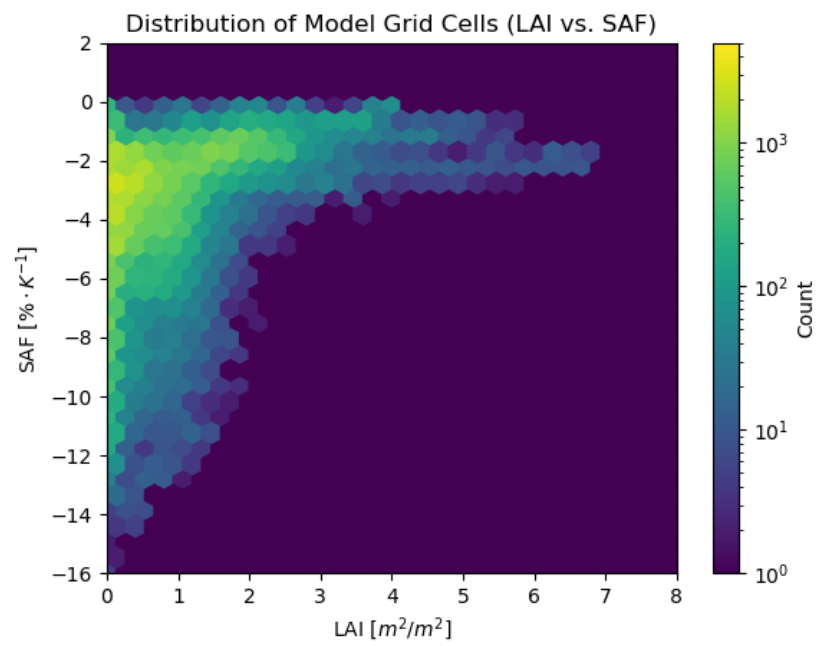
Figure 4.8: Relationship between LAI and SAF for all models, plotted as a density histogram.
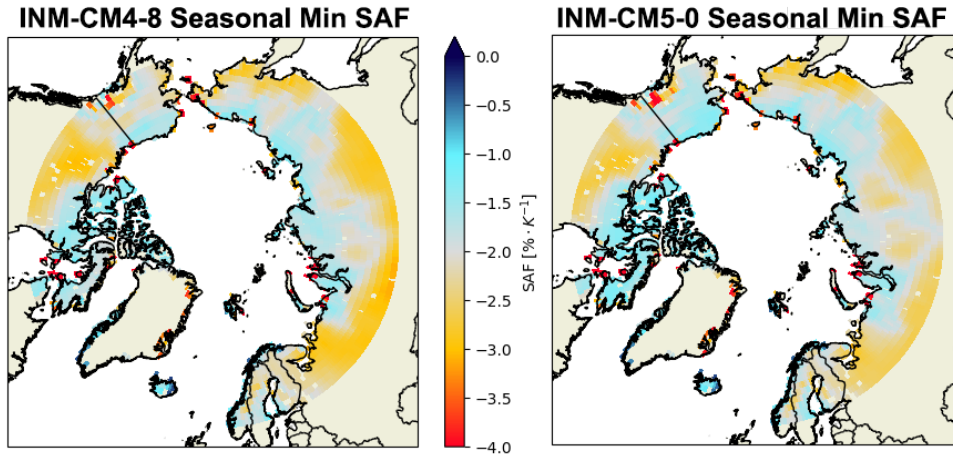
Figure 4.9: Spatial plot of minimum SAF over the seasonal cycle for INM-CM4-8 and INM-CM5-0.

$$\text{SAF(LAI)} = a \cdot \log(\text{LAI}) + b \tag{4.2}$$

We note that the fit parameters a, b characterizing the logarithmic relationship between LAI and SAF differ considerably between models (shown in Table 4.2). This demonstrates that we also have spread on the functional relationship between LAI and SAF between models, and that the vegetation-driven spread in SAF is not simply due to different LAI inputs, but also results from differences in how models parameterize albedo as a function of LAI.

We have also identified two outliers from the same modelling group, INM-CM4-8 and INM-CM5-0, which show a completely different relationship between LAI and SAF. Given that the MODIS dataset (shown as a solid black line in Fig.4.10) clearly establishes a positive relationship between LAI and SAF, we conclude that these models do not accurately represent the relationship between vegetation and SAF. In particular, we have investigated the spatial distribution of SAF for the INM models (shown in Fig.4.9), and we observe that the resulting SAF fields are spatially inconsistent with MODIS SAF results. In particular we find that the INM models show grassland and barren regions have lower SAF than forested regions, which is inconsistent with observational results.

In order to test the extent to which the LAI vs. SAF relationship is monotonic, we have performed a calculation of the Spearman rank correlation coefficient, the results

61

of which are shown in Table 4.2. We observe that for most models, the correlation is high, indicating a robust relationship between LAI and SAF. In general, the LAI-SAF relationship observed in these models is a result of how diverse models parametrize albedo as a function of surface vegetation. This indicates the need for additional diagnostics of the LAI-albedo parametrization on outlier models such as INM-CM4-8, INM-CM5-0 and CMCC-CM2-HR4.
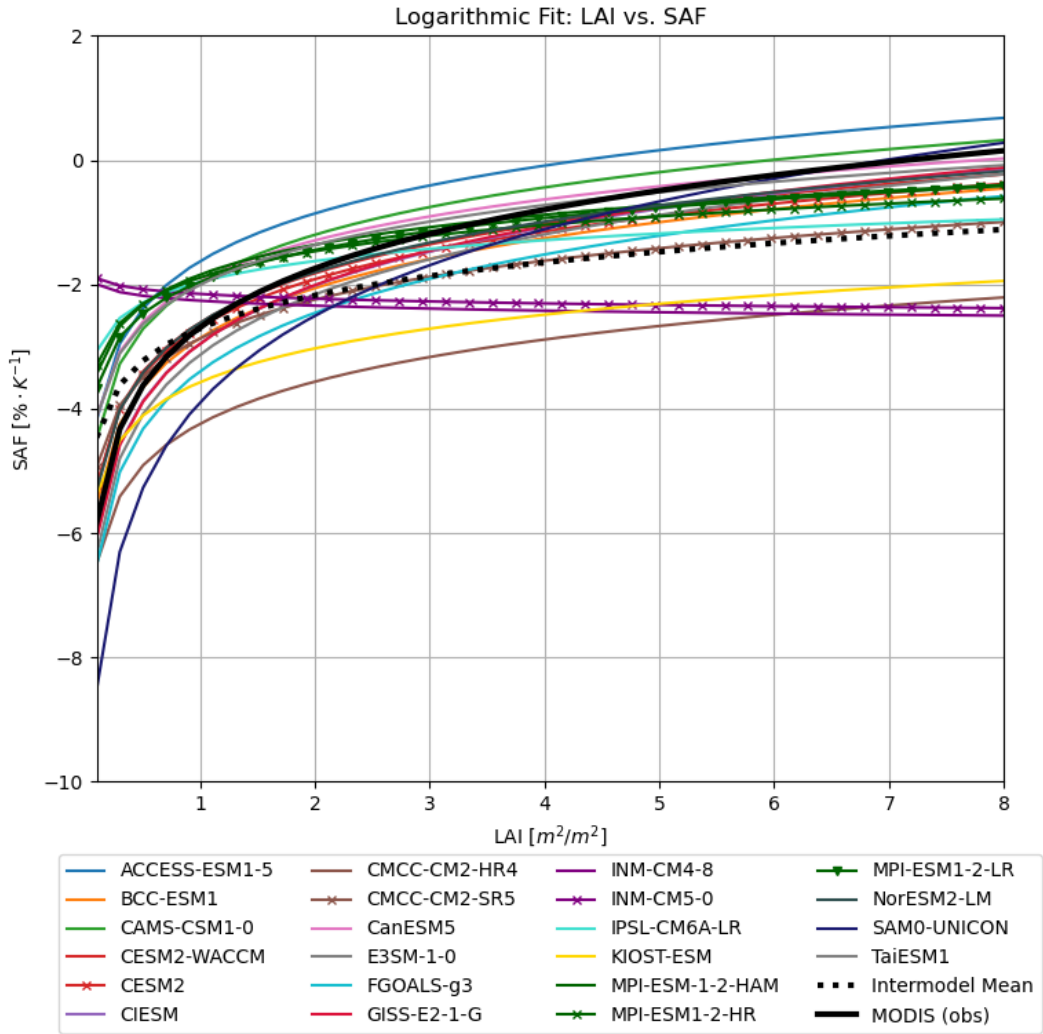
Figure 4.10: Relationship between LAI and SAF, with each model fit to a logarithmic function of the form $f(x) = a \log(x) + b$.

Model	a	Δa	b	Δb	Spearman R
ACCESS-ESM1-5	1.1094	0.0337	-1.6281	0.0357	0.834
BCC-ESM1	1.1573	0.0389	-2.8628	0.0351	0.805
CAMS-CSM1-0	1.099	0.0382	-1.9642	0.0399	0.827
CESM2-WACCM	1.1478	0.0494	-2.6167	0.0475	0.781
CESM2	1.107	0.0487	-2.6839	0.0461	0.776
CIESM	1.3463	0.0951	-2.9524	0.0664	0.488
CMCC-CM2-HR4	0.9776	0.1233	-4.2431	0.0769	0.278
CMCC-CM2-SR5	0.9007	0.0478	-2.8683	0.0456	0.655
CanESM5	0.9496	0.0324	-1.9507	0.0468	0.777
E3SM-1-0	1.3964	0.072	-3.1311	0.0654	0.547
FGOALS-g3	1.3554	0.1235	-3.3983	0.0689	0.37
GISS-E2-1-G	1.3637	0.0899	-2.9559	0.0648	0.527
INM-CM4-8	-0.1154	0.0299	-2.263	0.0312	-0.257
INM-CM5-0	-0.11	0.0297	-2.154	0.0295	-0.286
IPSL-CM6A-LR	0.4844	0.0333	-1.9615	0.0367	0.547
KIOST-ESM	0.7835	0.0596	-3.5736	0.0694	0.647
MPI-ESM-1-2-HAM	0.6947	0.0303	-1.8437	0.0314	0.736
MPI-ESM1-2-HR	0.6116	0.0254	-1.8907	0.0231	0.806
MPI-ESM1-2-LR	0.7415	0.0296	-1.9599	0.027	0.824
NorESM2-LM	1.1727	0.0452	-2.6169	0.0492	0.82
SAM0-UNICON	2.0091	0.1512	-3.8994	0.1007	0.477
TaiESM1	0.9249	0.0538	-2.0063	0.0607	0.734
Intermodel Mean	0.764	0.017	-2.706	0.016	0.4678
MODIS (obs)	1.367	0.001	-2.691	0.001	0.2885

Table 4.2: Statistics for logarithmic fit coefficients, along with error signifying 95% confidence interval $(a - \Delta a, a + \Delta a)$ and correlation coefficient. These coefficients were fit to a logarithmic curve for each model using a weighted least-squares fit in MATLAB. The Spearman rank coefficients represent the monotonicity of the relationship between LAI and SAF for each model.

Chapter 5

Conclusions

Radiative feedback processes such as Arctic amplification are key drivers of climate change. In this work, we have demonstrated using MODIS remote sensing data that SAF is stronger than predicted by the CMIP6 ensemble of climate models. Furthermore, we were able to identify that this discrepancy is primarily due to strong feedbacks in high-Arctic grassland and barren regions. Using high-resolution remote sensing data, we show that SAF in these vegetation zones is as strong as $-16\% \cdot K^{-1}$ in certain regions of Nunavut and Siberia. These features are present in areas of complex local topography which model grid sizes are insufficient to resolve. Our observational results are consistent with the previous literature once we account for differences in methodology. In this work, we use a restricted spatial domain (we analyze all land north of 60°N, as opposed to 45°N in previous work) and extend the SAF analysis to July-August in order to capture late season melt-off.

We found that vegetation subtype exerts a strong influence on surface albedo, and by extension SAF. We have extended the results of Loranty (2016) [1] to show that for a given vegetation type, the seasonal cycle of albedo is logistic in nature. However, the large spatial variability within vegetation subtypes necessitates the use of additional vegetation predictors such as LAI, as vegetation subtype is insufficient on its own as a predictor.

Using an analytic decomposition, we were able to provide indirect evidence for changes in albedo linked to shifts in land cover. However, the magnitude of this effect (10% of the total SAF change for June-July can be attributed to land cover changes) was smaller than anticipated.

The influence of resolution on error in resolving SAF was a key focus of this work. Current climate models such as the Community Land Model (CLM) [53] address subgrid dynamics by using a fractional partitioning scheme for each grid cell. Given that the

SAF depends on the interaction between two high-resolution fields (vegetation and snow cover), the fractional scheme cannot fully account for high-resolution detail. We have demonstrated that the mean local upscaling error for an 100km model grid cell is large, reaching $0.773\% \cdot K^{-1}$ for June-July, indicating considerable variability at spatial scales smaller than 100km. However, we found a cancellation of errors when applied to the pan-Arctic mean SAF, yielding a global error of $\Delta NET = 0.058\% \cdot K^{-1}$. This indicates that while there is large variability in SAF at local scales, due to cancellation of errors, using low-resolution albedo fields does not introduce significant error to the pan-Arctic mean SAF.

By performing a comparison between observational data and the CMIP6 ensemble we found that between 60N and 70N, the intermodel mean LAI is much larger than the MODIS results. This indicates that the CMIP6 ensemble is currently over-estimating LAI for evergreen forests. Additionally, we demonstrate that LAI provides a key constraint on the maximum strength of the SAF, with forested regions showing much lower SAF than barren or grassland regions. Specifically, LAI and SAF show a logarithmic relationship, with saturation occurring for high LAI values.

Given the ongoing relevance of SAF to Arctic warming, and the large spread in the SAF for CMIP6 models, our work provides clear motivation for further investigation of model vegetation-albedo parametrizations, in order to better constrain the spread on the SAF.

5.1 Future Work

A key focus of this work was investigating the influence of resolution on SAF errors. Although we have shown that increasing the resolution of albedo fields does not significantly change the result for pan-Arctic mean SAF, this leaves open the possibility that there are high-resolution interactions at sub-model grid scales between vegetation fields (vegetation subtype, LAI) and snow cover which yield global errors in SAF. One possible investigation would be to start with a parametrization scheme for albedo as a function of vegetation and snow cover, and explore the impact of increasing resolution on both local and global errors in albedo.

One of the research questions in this work was the extent to which changes in vegetation impact SAF. We propose an extension of this investigation via model simulations by extending the methods used in [3] in order to apply a prescribed vegetation field to a climate model. This would provide a clearer understanding on the impacts of dynamic vegetation on SAF.

66

References

[1] Michael M. Loranty, Scott J. Goetz, and Pieter S. A. Beck. Tundra vegetation effects on pan-Arctic albedo. Environmental Research Letters, 6(2):024014, April 2011. Publisher: IOP Publishing.

[2] Xin Qu and Alex Hall. What Controls the Strength of Snow-Albedo Feedback? Journal of Climate, 20(15):3971–3981, August 2007. Publisher: American Meteorological Society.

[3] Libo Wang, Jason N. S. Cole, Paul Bartlett, Diana Verseghy, Chris Derksen, Ross Brown, and Knut von Salzen. Investigating the spread in surface albedo for snow-covered forests in CMIP5 models. Journal of Geophysical Research: Atmospheres, 121(3):1104–1119, 2016. _eprint: https://agupubs.onlinelibrary.wiley.com/doi/pdf/10.1002/2015JD023824.

[4] Eric Post, Richard B. Alley, Torben R. Christensen, Marc Macias-Fauria, Bruce C. Forbes, Michael N. Gooseff, Amy Iler, Jeffrey T. Kerby, Kristin L. Laidre, Michael E. Mann, Johan Olofsson, Julienne C. Stroeve, Fran Ulmer, Ross A. Virginia, and Muyin Wang. The polar regions in a 2℃ warmer world. Science Advances, 5(12):eaaw9883, December 2019. Publisher: American Association for the Advancement of Science Section: Review.

[5] James A. Screen and Ian Simmonds. The central role of diminishing sea ice in recent Arctic temperature amplification. Nature, 464(7293):1334–1337, April 2010. Place: London Publisher: Nature Publishing Group WOS:000277149000043.

[6] Hamish D. Pritchard, Robert J. Arthern, David G. Vaughan, and Laura A. Edwards. Extensive dynamic thinning on the margins of the Greenland and Antarctic ice sheets. Nature, 461(7266):971–975, October 2009. Place: London Publisher: Nature Publishing Group WOS:000270817700045.

[7] Christopher G. Fletcher, Hongxu Zhao, Paul J. Kushner, and Richard Fernandes. Using models and satellite observations to evaluate the strength of snow albedo feedback. Journal of Geophysical Research: Atmospheres, 117(D11), 2012. _eprint: https://agupubs.onlinelibrary.wiley.com/doi/pdf/10.1029/2012JD017724.

[8] Xin Qu and Alex Hall. On the persistent spread in snow-albedo feedback. Climate Dynamics, 42(1-2):69–81, January 2014.

[9] Shunlin Liang, Alan H. Strahler, and Charles Walthall. Retrieval of Land Surface Albedo from Satellite Observations: A Simulation Study. Journal of Applied Meteorology and Climatology, 38(6):712–725, June 1999. Publisher: American Meteorological Society Section: Journal of Applied Meteorology and Climatology.

[10] Christian A. Gueymard, Vicente Lara-Fanego, Manajit Sengupta, and Yu Xie. Surface albedo and reflectance: Review of definitions, angular and spectral effects, and intercomparison of major data sources in support of advanced solar irradiance modeling over the Americas. Solar Energy, 182:194–212, April 2019.

[11] C. Matzler. On the determination of surface emissivity from satellite observations. Ieee Geoscience and Remote Sensing Letters, 2(2):160–163, April 2005. Place: Piscataway Publisher: Ieee-Inst Electrical Electronics Engineers Inc WOS:000230796000015.

[12] W. Zhang, P. A. Miller, C. Jansson, P. Samuelsson, J. Mao, and B. Smith. Self-Amplifying Feedbacks Accelerate Greening and Warming of the Arctic. Geophysical Research Letters, 45(14):7102–7111, July 2018. Place: Washington Publisher: Amer Geophysical Union WOS:000442582100039.

[13] Jm Chen and Ta Black. Defining Leaf-Area Index for Non-Flat Leaves. Plant Cell and Environment, 15(4):421–429, May 1992. Place: Oxford Publisher: Blackwell Science Ltd WOS:A1992HV62900005.

[14] Libo Wang, Paul Bartlett, Darren Pouliot, Ed Chan, Celine Lamarche, Michael A. Wulder, Pierre Defourny, and Mike Brady. Comparison and Assessment of Regional and Global Land Cover Datasets for Use in CLASS over Canada. Remote Sensing, 11(19):2286, October 2019. Place: Basel Publisher: Mdpi WOS:000496827100100.

[15] Quentin Lejeune, Edouard L. Davin, Grégory Duveiller, Bas Crezee, Ronny Meier, Alessandro Cescatti, and Sonia I. Seneviratne. Biases in the albedo sensitivity to deforestation in CMIP5 models and their impacts on the associated historical radiative forcing. Earth System Dynamics, 11(4):1209–1232, December 2020. Publisher: Copernicus GmbH.

[16] Jayme A. Prevedello, Gisele R. Winck, Marcelo M. Weber, Elizabeth Nichols, and Barry Sinervo. Impacts of forestation and deforestation on local temperature across the globe. PLOS ONE, 14(3):e0213368, March 2019. Publisher: Public Library of Science.

[17] Robert R. Pattison, Janet C. Jorgenson, Martha K. Raynolds, and Jeffery M. Welker. Trends in NDVI and Tundra Community Composition in the Arctic of NE Alaska Between 1984 and 2009. Ecosystems, 18(4):707–719, June 2015.

[18] Lin Zhao, Aiguo Dai, and Bo Dong. Changes in global vegetation activity and its driving factors during 1982-2013. Agricultural and Forest Meteorology, 249:198–209, February 2018. Place: Amsterdam Publisher: Elsevier Science Bv WOS:000424180100017.

[19] Daan Blok, Gabriela Schaepman-Strub, Harm Bartholomeus, Monique M P D Heijmans, Trofim C Maximov, and Frank Berendse. The response of Arctic vegetation to the summer climate: relation between shrub cover, NDVI, surface albedo and temperature. Environmental Research Letters, 6(3):035502, July 2011.

[20] Richard G. Pearson, Steven J. Phillips, Michael M. Loranty, Pieter S. A. Beck, Theodoros Damoulas, Sarah J. Knight, and Scott J. Goetz. Shifts in Arctic vegetation and associated feedbacks under climate change. Nature Climate Change, 3(7):673–677, July 2013. Number: 7 Publisher: Nature Publishing Group.

[21] Bruce C. Forbes, Marc Macias Fauria, and Pentti Zetterberg. Russian Arctic warming and 'greening' are closely tracked by tundra shrub willows. Global Change Biology, 16(5):1542–1554, May 2010. Place: Hoboken Publisher: Wiley WOS:000276696100010.

[22] Chad W. Thackeray, Christopher G. Fletcher, and Chris Derksen. The influence of canopy snow parameterizations on snow albedo feedback in boreal forest regions. Journal of Geophysical Research: Atmospheres, 119(16):9810–9821, 2014. _eprint: https://onlinelibrary.wiley.com/doi/pdf/10.1002/2014JD021858.

[23] Chad W. Thackeray, Christopher G. Fletcher, and Chris Derksen. Diagnosing the Impacts of Northern Hemisphere Surface Albedo Biases on Simulated Climate. Journal of Climate, 32(6):1777–1795, March 2019. Place: Boston Publisher: Amer Meteorological Soc WOS:000460531600001.

[24] G. Danabasoglu, J.-F. Lamarque, J. Bacmeister, D. A. Bailey, A. K. DuVivier, J. Edwards, L. K. Emmons, J. Fasullo, R. Garcia, A. Gettelman, C. Hannay, M. M. Holland,

W. G. Large, P. H. Lauritzen, D. M. Lawrence, J. T. M. Lenaerts, K. Lindsay, W. H. Lipscomb, M. J. Mills, R. Neale, K. W. Oleson, B. Otto-Bliesner, A. S. Phillips, W. Sacks, S. Tilmes, L. van Kampenhout, M. Vertenstein, A. Bertini, J. Dennis, C. Deser, C. Fischer, B. Fox-Kemper, J. E. Kay, D. Kinnison, P. J. Kushner, V. E. Larson, M. C. Long, S. Mickelson, J. K. Moore, E. Nienhouse, L. Polvani, P. J. Rasch, and W. G. Strand. The Community Earth System Model Version 2 (CESM2). Journal of Advances in Modeling Earth Systems, 12(2):e2019MS001916, 2020. _eprint: https://onlinelibrary.wiley.com/doi/pdf/10.1029/2019MS001916.

[25] David M. Lawrence, Rosie A. Fisher, Charles D. Koven, Keith W. Oleson, Sean C. Swenson, Gordon Bonan, Nathan Collier, Bardan Ghimire, Leo van Kampenhout, Daniel Kennedy, Erik Kluzek, Peter J. Lawrence, Fang Li, Hongyi Li, Danica Lombardozzi, William J. Riley, William J. Sacks, Mingjie Shi, Mariana Vertenstein, William R. Wieder, Chonggang Xu, Ashehad A. Ali, Andrew M. Badger, Gautam Bisht, Michiel van den Broeke, Michael A. Brunke, Sean P. Burns, Jonathan Buzan, Martyn Clark, Anthony Craig, Kyla Dahlin, Beth Drewniak, Joshua B. Fisher, Mark Flanner, Andrew M. Fox, Pierre Gentine, Forrest Hoffman, Gretchen Keppel-Aleks, Ryan Knox, Sanjiv Kumar, Jan Lenaerts, L. Ruby Leung, William H. Lipscomb, Yaqiong Lu, Ashutosh Pandey, Jon D. Pelletier, Justin Perket, James T. Randerson, Daniel M. Ricciuto, Benjamin M. Sanderson, Andrew Slater, Zachary M. Subin, Jinyun Tang, R. Quinn Thomas, Maria Val Martin, and Xubin Zeng. The Community Land Model Version 5: Description of New Features, Benchmarking, and Impact of Forcing Uncertainty. Journal of Advances in Modeling Earth Systems, 11(12):4245–4287, December 2019. Place: Washington Publisher: Amer Geophysical Union WOS:000502568600001.

[26] Ronny Meier, Edouard L. Davin, Quentin Lejeune, Mathias Hauser, Yan Li, Brecht Martens, Natalie M. Schultz, Shannon Sterling, and Wim Thiery. Evaluating and improving the Community Land Model's sensitivity to land cover. Biogeosciences, 15(15):4731–4757, August 2018. Publisher: Copernicus GmbH.

[27] Gordon B. Bonan, Edward G. Patton, John J. Finnigan, Dennis D. Baldocchi, and Ian N. Harman. Moving beyond the incorrect but useful paradigm: reevaluating big-leaf and multilayer plant canopies to model biosphere-atmosphere fluxes - a review. Agricultural and Forest Meteorology, 306:108435, August 2021. Place: Amsterdam Publisher: Elsevier WOS:000659137200003.

[28] Ronny Meier, Edouard L. Davin, Gordon B. Bonan, David M. Lawrence, Xiaolong Hu, Gregory Duveiller, Catherine Prigent, and Sonia Seneviratne. Impacts of a revised

surface roughness parameterization in the Community Land Model 5.1. <u>Geoscientific Model Development</u>, 15(6):2365–2393, March 2022. Place: Gottingen Publisher: Copernicus Gesellschaft Mbh WOS:000773390800001.

[29] Richard Essery. Large-scale simulations of snow albedo masking by forests. <u>Geophysical Research Letters</u>, 40(20):5521–5525, 2013. _eprint: https://agupubs.onlinelibrary.wiley.com/doi/pdf/10.1002/grl.51008.

[30] Shilong Piao, Xuhui Wang, Taejin Park, Chi Chen, Xu Lian, Yue He, Jarle W. Bjerke, Anping Chen, Philippe Ciais, Hans Tommervik, Ramakrishna R. Nemani, and Ranga B. Myneni. Characteristics, drivers and feedbacks of global greening. <u>Nature Reviews Earth & Environment</u>, 1(1):14–27, January 2020. Place: London Publisher: Springernature WOS:000649235000011.

[31] Andreas Roesch and Erich Roeckner. Assessment of Snow Cover and Surface Albedo in the ECHAM5 General Circulation Model. <u>Journal of Climate</u>, 19(16):3828–3843, August 2006. Publisher: American Meteorological Society Section: Journal of Climate.

[32] F. Mark Danson, David Hetherington, Felix Morsdorf, Benjamin Koetz, and Britta Allgower. Forest Canopy Gap Fraction From Terrestrial Laser Scanning. <u>IEEE Geoscience and Remote Sensing Letters</u>, 4(1):157–160, January 2007. Conference Name: IEEE Geoscience and Remote Sensing Letters.

[33] Chad W. Thackeray, Xin Qu, and Alex Hall. Why Do Models Produce Spread in Snow Albedo Feedback? <u>Geophysical Research Letters</u>, 45(12):6223–6231, 2018. _eprint: https://onlinelibrary.wiley.com/doi/pdf/10.1029/2018GL078493.

[34] Chad W. Thackeray, Christopher G. Fletcher, and Chris Derksen. Quantifying the skill of CMIP5 models in simulating seasonal albedo and snow cover evolution. <u>Journal of Geophysical Research-Atmospheres</u>, 120(12):5831–5849, June 2015. Place: Washington Publisher: Amer Geophysical Union WOS:000357956800007.

[35] Alex Hall and Xin Qu. Using the current seasonal cycle to constrain snow albedo feedback in future climate change. <u>Geophysical Research Letters</u>, 33(3), 2006. _eprint: https://agupubs.onlinelibrary.wiley.com/doi/pdf/10.1029/2005GL025127.

[36] Chad W. Thackeray, Alex Hall, Mark D. Zelinka, and Christopher G. Fletcher. Assessing Prior Emergent Constraints on Surface Albedo Feedback in CMIP6. <u>Journal of Climate</u>, 34(10):3889–3905, May 2021. Place: Boston Publisher: Amer Meteorological Soc WOS:000644153200010.

[37] Mark S. Williamson, Chad W. Thackeray, Peter M. Cox, Alex Hall, Chris Huntingford, and Femke J. M. M. Nijsse. Emergent constraints on climate sensitivities. Reviews of Modern Physics, 93(2):025004, May 2021. Place: College Pk Publisher: Amer Physical Soc WOS:000655978800001.

[38] Chad W. Thackeray and Alex Hall. An emergent constraint on future Arctic sea-ice albedo feedback. Nature Climate Change, 9(12):972–+, December 2019. Place: London Publisher: Nature Publishing Group WOS:000499106300024.

[39] M. A. Friedl, D. K. McIver, J. C. F. Hodges, X. Y. Zhang, D. Muchoney, A. H. Strahler, C. E. Woodcock, S. Gopal, A. Schneider, A. Cooper, A. Baccini, F. Gao, and C. Schaaf. Global land cover mapping from MODIS: algorithms and early results. Remote Sensing of Environment, 83(1-2):287–302, November 2002. Place: New York Publisher: Elsevier Science Inc WOS:000179160200019.

[40] Vincent V. Salomonson, William Barnes, and Edward J. Masuoka. Introduction to MODIS and an Overview of Associated Activities. In John J. Qu, Wei Gao, Menas Kafatos, Robert E. Murphy, and Vincent V. Salomonson, editors, Earth Science Satellite Remote Sensing: Vol. 1: Science and Instruments, pages 12–32. Springer, Berlin, Heidelberg, 2006.

[41] MOD43B3 Albedo Product - UMass Boston.

[42] Fanglin Yang, Kenneth Mitchell, Yu-Tai Hou, Yongjiu Dai, Xubin Zeng, Zhuo Wang, and Xin-Zhong Liang. Dependence of Land Surface Albedo on Solar Zenith Angle: Observations and Model Parameterization. Journal of Applied Meteorology and Climatology, 47(11):2963–2982, November 2008. Publisher: American Meteorological Society Section: Journal of Applied Meteorology and Climatology.

[43] B. Poulter, N. MacBean, A. Hartley, I. Khlystova, O. Arino, R. Betts, S. Bontemps, M. Boettcher, C. Brockmann, P. Defourny, S. Hagemann, M. Herold, G. Kirches, C. Lamarche, D. Lederer, C. Ottlé, M. Peters, and P. Peylin. Plant functional type classification for earth system models: results from the European Space Agency's Land Cover Climate Change Initiative. Geoscientific Model Development, 8(7):2315–2328, July 2015. Publisher: Copernicus GmbH.

[44] Veronika Eyring, Sandrine Bony, Gerald A. Meehl, Catherine A. Senior, Bjorn Stevens, Ronald J. Stouffer, and Karl E. Taylor. Overview of the Coupled Model Intercomparison Project Phase 6 (CMIP6) experimental design and organization. Geoscientific Model Development, 9(5):1937–1958, May 2016. Publisher: Copernicus GmbH.

[45] Masoud Hessami, Philippe Gachon, Taha B. M. J. Ouarda, and Andre St-Hilaire. Automated regression-based statistical downscaling tool. Environmental Modelling & Software, 23(6):813–834, June 2008. Place: Oxford Publisher: Elsevier Sci Ltd WOS:000254144000011.

[46] R. Manzanas, J. M. Gutierrez, J. Fernandez, E. van Meijgaard, S. Calmanti, M. E. Magarino, A. S. Cofino, and S. Herrera. Dynamical and statistical downscaling of seasonal temperature forecasts in Europe: Added value for user applications. Climate Services, 9:44–56, January 2018. Place: Amsterdam Publisher: Elsevier WOS:000582007400005.

[47] James Munkres. Topology. Pearson Education, 2014. Accepted: 2018-01-08T01:53:14Z.

[48] Donald A. Walker, Martha K. Raynolds, Fred J. A. Daniëls, Eythor Einarsson, Arve Elvebakk, William A. Gould, Adrian E. Katenin, Sergei S. Kholod, Carl J. Markon, Evgeny S. Melnikov, Natalia G. Moskalenko, Stephen S. Talbot, Boris A. (†) Yurtsev, and The other members of the CAVM Team. The Circumpolar Arctic vegetation map. Journal of Vegetation Science, 16(3):267–282, 2005. _eprint: https://onlinelibrary.wiley.com/doi/pdf/10.1111/j.1654-1103.2005.tb02365.x.

[49] John Dwyer and Gail Schmidt. The MODIS Reprojection Tool. In John J. Qu, Wei Gao, Menas Kafatos, Robert E. Murphy, and Vincent V. Salomonson, editors, Earth Science Satellite Remote Sensing: Vol. 2: Data, Computational Processing, and Tools, pages 162–177. Springer, Berlin, Heidelberg, 2006.

[50] Xiaoning Zhang, Ziti Jiao, Changsen Zhao, Ying Qu, Qiang Liu, Hu Zhang, Yidong Tong, Chenxia Wang, Sijie Li, Jing Guo, Zidong Zhu, Siyang Yin, and Lei Cui. Review of Land Surface Albedo: Variance Characteristics, Climate Effect and Management Strategy. Remote Sensing, 14(6):1382, January 2022. Number: 6 Publisher: Multidisciplinary Digital Publishing Institute.

[51] V. L. Semerikov and M. Lascoux. Genetic relationship among Eurasian and American Larix species based on allozymes. Heredity, 83:62–70, July 1999. Patent Number: 1 Place: London Publisher: Nature Publishing Group WOS:000081751500008.

[52] X. X. Wei and X. Q. Wang. Phylogenetic split of Larix: evidence from paternally inherited cpDNA trnT-trnF region. Plant Systematics and Evolution, 239(1-2):67–77, July 2003. Place: Vienna Publisher: Springer-Verlag Wien WOS:000184452600005.

[53] Keith W. Oleson, Gordon B. Bonan, Crystal Schaaf, Feng Gao, Yufang Jin, and Alan Strahler. Assessment of global climate model land surface albedo using MODIS data. Geophysical Research Letters, 30(8), 2003. _eprint: https://agupubs.onlinelibrary.wiley.com/doi/pdf/10.1029/2002GL016749.

[54] Richard Fernandes, Hongxu Zhao, Xuanji Wang, Jeff Key, Xin Qu, and Alex Hall. Controls on Northern Hemisphere snow albedo feedback quantified using satellite Earth observations. Geophysical Research Letters, 36(21), 2009. _eprint: https://agupubs.onlinelibrary.wiley.com/doi/pdf/10.1029/2009GL040057.

[55] Christopher G. Fletcher, Chad W. Thackeray, and Tonya M. Burgers. Evaluating biases in simulated snow albedo feedback in two generations of climate models. Journal of Geophysical Research: Atmospheres, 120(1):12–26, 2015. _eprint: https://agupubs.onlinelibrary.wiley.com/doi/pdf/10.1002/2014JD022546.

[56] Chad W. Thackeray and Christopher G. Fletcher. Snow albedo feedback: Current knowledge, importance, outstanding issues and future directions. Progress in Physical Geography: Earth and Environment, 40(3):392–408, June 2016. Publisher: SAGE Publications Ltd.

[57] James Maslanik, Charles Fowler, Jeffrey Key, Ted Scambos, Todd Hutchinson, and William Emery. AVHRR-based Polar Pathfinder products for modeling applications. Annals of Glaciology, 25:388–392, 1997. Publisher: Cambridge University Press.

[58] Yunping Chen, Shuaifeng Jiao, Yuanlei Cheng, Haichang Wei, Lin Sun, and Yuan Sun. LAI-NOS: An automatic network observation system for leaf area index based on hemispherical photography. Agricultural and Forest Meteorology, 322:108999, July 2022. Place: Amsterdam Publisher: Elsevier WOS:000805255100001.

[59] Ralf Döscher, Mario Acosta, Andrea Alessandri, Peter Anthoni, Thomas Arsouze, Tommi Bergman, Raffaele Bernardello, Souhail Boussetta, Louis-Philippe Caron, Glenn Carver, Miguel Castrillo, Franco Catalano, Ivana Cvijanovic, Paolo Davini, Evelien Dekker, Francisco J. Doblas-Reyes, David Docquier, Pablo Echevarria, Uwe Fladrich, Ramon Fuentes-Franco, Matthias Gröger, Jost v. Hardenberg, Jenny Hieronymus, M. Pasha Karami, Jukka-Pekka Keskinen, Torben Koenigk, Risto Makkonen, François Massonnet, Martin Ménégoz, Paul A. Miller, Eduardo Moreno-Chamarro, Lars Nieradzik, Twan van Noije, Paul Nolan, Declan O'Donnell, Pirkka Ollinaho, Gijs van den Oord, Pablo Ortega, Oriol Tintó Prims, Arthur Ramos, Thomas Reerink, Clement Rousset, Yohan Ruprich-Robert, Philippe Le Sager, Torben

Schmith, Roland Schrödner, Federico Serva, Valentina Sicardi, Marianne Sloth Madsen, Benjamin Smith, Tian Tian, Etienne Tourigny, Petteri Uotila, Martin Vancoppenolle, Shiyu Wang, David Wårlind, Ulrika Willén, Klaus Wyser, Shuting Yang, Xavier Yepes-Arbós, and Qiong Zhang. The EC-Earth3 Earth system model for the Coupled Model Intercomparison Project 6. Geoscientific Model Development, 15(7):2973–3020, April 2022. Publisher: Copernicus GmbH.

[60] Ahmed M. El Kenawy, Mohamed E. Hereher, and Sayed M. Robaa. An Assessment of the Accuracy of MODIS Land Surface Temperature over Egypt Using Ground-Based Measurements. Remote Sensing, 11(20):2369, January 2019. Number: 20 Publisher: Multidisciplinary Digital Publishing Institute.